



HAL
open science

Episodic reactivation of carbonate fault zones with implications for permeability – An example from Provence, Southeast France

Rodrigo S.M. Corrêa, Estibalitz Ukar, Stephen Laubach, Irène Aubert, Juliette Lamarche, Qiqi Wang, Daniel Stockli, Lisa Stockli, Toti Larson

► To cite this version:

Rodrigo S.M. Corrêa, Estibalitz Ukar, Stephen Laubach, Irène Aubert, Juliette Lamarche, et al.. Episodic reactivation of carbonate fault zones with implications for permeability – An example from Provence, Southeast France. *Marine and Petroleum Geology*, 2022, 145, pp.105905. 10.1016/j.marpetgeo.2022.105905 . hal-03873247

HAL Id: hal-03873247

<https://hal.science/hal-03873247>

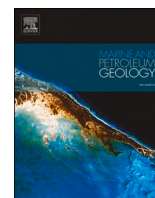
Submitted on 28 Nov 2022

HAL is a multi-disciplinary open access archive for the deposit and dissemination of scientific research documents, whether they are published or not. The documents may come from teaching and research institutions in France or abroad, or from public or private research centers.

L'archive ouverte pluridisciplinaire **HAL**, est destinée au dépôt et à la diffusion de documents scientifiques de niveau recherche, publiés ou non, émanant des établissements d'enseignement et de recherche français ou étrangers, des laboratoires publics ou privés.



Distributed under a Creative Commons Attribution - NonCommercial 4.0 International License



Episodic reactivation of carbonate fault zones with implications for permeability – An example from Provence, Southeast France

Rodrigo S.M. Corrêa^{a,b,c,*}, Estibalitz Ukar^b, Stephen E. Laubach^b, Irène Aubert^d, Juliette Lamarche^d, Qiqi Wang^{a,b}, Daniel F. Stockli^a, Lisa D. Stockli^a, Toti E. Larson^b

^a Department of Geological Sciences, The University of Texas at Austin, 2275 Speedway Stop C9000, Austin, TX, 78712, USA

^b Bureau of Economic Geology, The University of Texas at Austin, 10100 Burnet Road, Austin, TX, 78713, USA

^c Petrobras S.A., Avenida Henrique Valadares, 28, Rio de Janeiro, RJ, 20231-030, Brazil

^d Cerege Um 34, Aix-Marseille Université, 3 Place Victor Hugo (Case 67), 13331, Marseille Cedex 03, France

ARTICLE INFO

Keywords:

Opening-mode fracture
Calcite cement
Diagenesis
U–Pb geochronology
Fault reactivation
Stable isotope geochemistry
Fluid flow
Veins

ABSTRACT

Exposed in large, continuous outcrops in Provence, southern France, the Castellans fault formed as a normal fault in the Upper Cretaceous and was reactivated as a left-lateral fault in the Eocene. Structural, petrographical, isotopic, and geochronological analyses shed light on the sequence of deformational-diagenetic stages of the fault zone and help identify properties that controlled fluid-flow behavior through time. Abrupt contrasts in fracture abundance compared to the undeformed host rock define a damage zone containing fractures arranged in regularly spaced clusters. We identified eleven episodes of calcite cementation within opening-mode fractures and host rock primary pores. Cement fabrics, sediment fills, and geochemistry show evidence of shallow burial environments. U–Pb geochronology of calcite cements indicate two main deformational phases of the fault zone during the Albo-Cenomanian Durancian uplift and Eocene Pyrenean orogeny at ca. 90 Ma and 50–40 Ma, respectively. Deformation created poro-permeability, but cementation followed shortly after, pervasively occluding most of the fault zone porosity by the end of the Eocene.

1. Introduction

Fault zones create spatial contrasts in porosity and permeability that affect fluid flow (Caine et al., 1996). Fault rocks may be highly deformed, forming conduits of increased permeability compared to the undeformed host rock (e.g. Evans et al., 1997; Billi et al., 2003; Kim et al., 2004; Bond et al., 2017), particularly along fracture corridors (e.g. Ozkaya, 2018; Bagni et al., 2020; Questiaux et al., 2010). On the one hand, open fractures may cause fluid channeling (e.g. Li et al., 2018), on the other hand cementation partially or completely occludes fluid-flow conduits (Aydin, 2000; Aydin and Eyal, 2002; Matonti et al., 2012). Understanding the origin, timing, and spatial arrangement of permo-porous heterogeneities in fault zones is relevant for access to fresh water, hydrocarbons, geothermal energy, and CO₂ storage (Caine et al., 1996; Kampman et al., 2012; Knipe et al., 1998; Underschultz et al., 2005; Bense et al., 2008; Laubach et al., 2019; Duwiquet et al., 2019).

Despite reducing reservoir porosity and permeability, cements are desirable as records of the deformation, diagenesis, and fluid conditions

acting at different points in time throughout the evolutionary history of a fault zone (Travé et al., 1997; Bussolotto et al., 2007; Lacroix et al., 2014; Aubert et al., 2019, 2020; Ferraro et al., 2019, 2020; Ukar et al., 2020; Muñoz-López et al., 2020; Cruset et al., 2020; Smeraglia et al., 2021). Cement textures, composition, crosscutting relationships, fracture intensity analysis around and away from fault cores, spatial arrangement, and geochronology can all be used to reconstruct the evolution of brittle deformation and associated poro-permeability (e.g. Hansman et al., 2018; Aubert et al., 2019, 2020, 2021; Cochard et al., 2021; Hoareau et al., 2021; Muñoz-López et al., 2022). Importantly, recent advances in calcite U–Pb geochronology allow direct dating of the absolute timing of calcite precipitation (Rasbury and Cole, 2009; Roberts et al., 2020; Roberts and Walker, 2016; Goodfellow et al., 2017; Holdsworth et al., 2019), opening an opportunity for in-depth structural-diagenetic studies of the evolutionary history of carbonate-rich fault zones (e.g. Hansman et al., 2018; Aubert et al., 2019, 2020, 2021; Cochard et al., 2021; Smeraglia et al., 2021; Hoareau et al., 2021; Muñoz-López et al., 2022). However, good exposures of carbonate fault zones that permit adequate analysis of all these characteristics are rare.

* Corresponding author. Department of Geological Sciences, The University of Texas at Austin, 2275 Speedway Stop C9000, Austin, TX, 78712, USA.
E-mail address: Rodrigo.correa@utexas.edu (R.S.M. Corrêa).

Here we describe the Castellás fault zone in SE France (Fig. 1), a reactivated normal to strike-slip fault with outstanding, 2 km-long continuous exposures where fracture spatial relationships and contacts with undeformed host rock can be readily observed. Previous studies (Matonti et al., 2012; Aubert et al., 2020) concluded that the Castellás fault shows several stages of deformation and cementation, but the absolute timing of events and their effect on fault permeability remain uncertain. We focus on the spatial arrangement of fractures in relation to the Castellás fault in the field, as well as small-scale structural, petrological, isotopic, and U–Pb geochronological analyses of fault core, damage zone and host rock cements to identify diagenetic and deformational events that controlled fluid flow behavior through time. We conclude that the fault zone underwent two main deformational events at ~90 Ma and 50–40 Ma, both of which created substantial poro-permeability before becoming a permanent barrier for fluid flow due to extensive calcite cementation near the end of the Eocene (Pyrenean orogeny).

2. Geological setting

2.1. Southeast France

The study area is in Provence, Southeast France, near the village of La Fare-les-Oliviers (Fig. 1a). The region experienced several tectonic events in a protracted geologic history reflected in complex fault and fracture patterns. The Southeast basin initially developed as a part of the Vocontian basin inside a passive margin of the former Tethys Ocean (Léonide et al., 2014). Environmental conditions allowed development of a large carbonate platform during the Jurassic and Early Cretaceous, including up to 800 m-thick deposits of Urgonian facies carbonate rocks (Masse, 1976; Bestani et al., 2015). The record of this succession has an overall shallowing-upward trend showing a broad facies variation from outer, mostly bioclastic and coral facies to rudist-dominated inner

platform environment (Cochard et al., 2021). The growth of the Urgonian platform ended due to a drowning event in the Aptian.

During Albian–Cenomanian time, the drift of the Iberian plate eastwards caused sinistral transtension and regional uplift characterized by a kilometric crustal bend followed by formation of a complex of horsts and grabens known as the Durance uplift (Guyonnet-Benaize et al., 2010; Bestani et al., 2015). This uplift was responsible for a marked erosional surface, tilting of the platform towards the south and creation of E–W trending normal faults (Guyonnet-Benaize et al., 2010; Aubert et al., 2019, 2020; Matonti et al., 2012), including the Castellás fault in its normal slip phase.

In the Late Cretaceous to Eocene, the area experienced a N–S contraction related to collision between Iberia and Europe (Pyrenean Orogeny). This event put SE France in a foreland position and caused new ENE–SSW structures marked by thrusts, folds, and strike-slip faults (Lamarche et al., 2012; Bestani et al., 2015). This new tectonic regime reactivated some old Durancian structures, including the Castellás fault, into left-lateral strike-slip faults (Matonti et al., 2012). During Oligocene to Miocene, extension in western Europe related to the drift of the Corsica–Sardinia continental block formed the Liguro–Provencal basin (Gattacceca et al., 2007). From the late Oligocene, the Alpine front propagated towards the Provence region due to regional N–S contraction also causing reactivation of older structures (Molliex et al., 2011). The prevalence of reactivation during this time decreases towards the south into the study area.

2.2. Castellás fault

In exceptionally complete, 2 km-long continuous exposures near La Fare-les-Oliviers, the Castellás fault cuts Lower Cretaceous Urgonian facies carbonate rocks (Fig. 1b). This N70E-trending, left-lateral strike-slip fault, originally formed as a normal fault during the Durancian uplift (Albian–Cenomanian), and was reactivated as a left-lateral, strike-

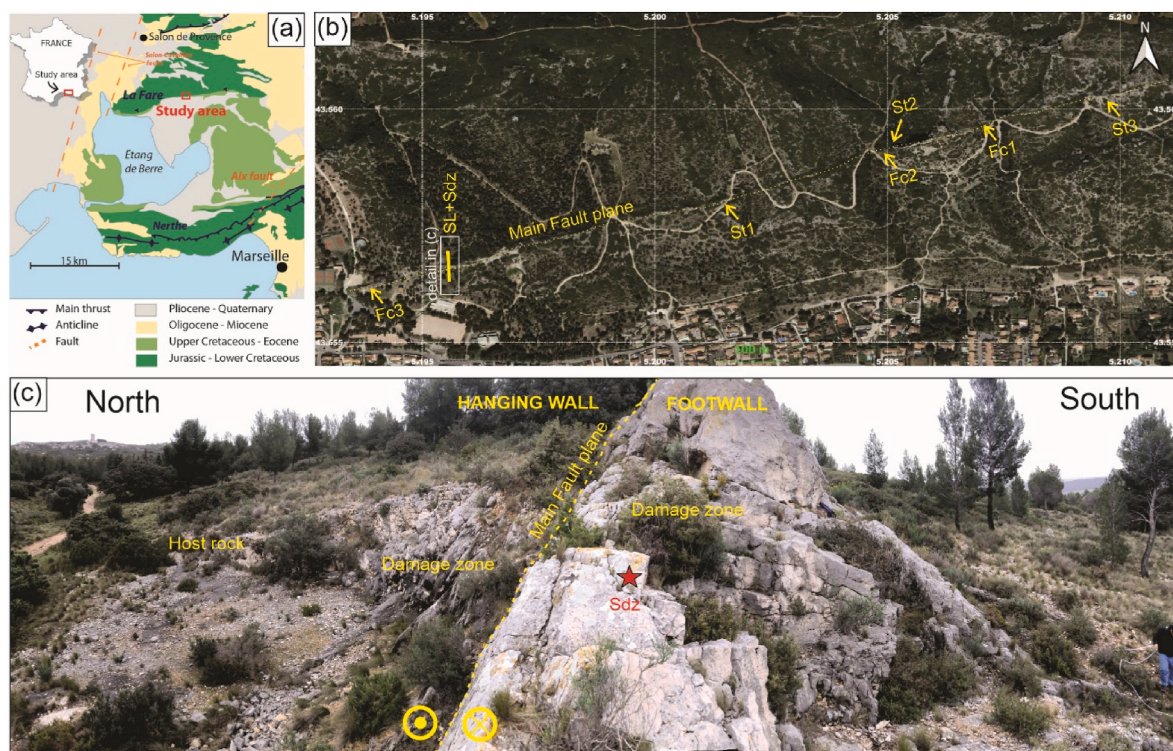


Fig. 1. Location and field photographs of the studied outcrop, near La Fare-les-Oliviers city, Southeast France ($43^{\circ} 33' 23.947''\text{N}$; $5^{\circ} 11' 43.595''\text{E}$). (a) Simplified geological map (modified from Aubert et al., 2019). (b) Aerial image of the Castellás fault with sample and scanline locations. Average trend of the scanline is $\text{N}15^{\circ}\text{E}$. (SL – Scanline trace, Fc – Fault core sample, St – Sampling transect). (c) Panoramic view of the outcrop showing the location of the main fault plane, damage zone and host rock, where the scanline was acquired (Sdz – Damage zone sample). Hanging wall on north side and footwall on south side.

slip fault during the Pyrenean orogeny (Matonti et al., 2012; Aubert et al., 2019). Due to this reactivation, the Castellás fault zone today shows two texturally distinct, mappable fault breccias, herein referred to as breccia 1 (BR1) of Durancian age, and breccia 2 (BR2) of Pyrenean age (Matonti et al., 2012). Also visible in outcrop are prominent sets of calcite-filled opening-mode fractures (i.e. calcite veins) spatially associated with the main fault (Fig. 2).

The Castellás fault is composed of several smaller coalesced fault segments arranged in an anastomosing pattern (Aubert, 2020) (Fig. 2a). Initial normal displacement of the Castellás fault and presence of BR1 are visible only in some parts of the fault zone; evidence of the normal phase of fault slip is therefore sporadic and localized (Aubert, 2020). Additional fault movement due to strike-slip reactivation led to overprinting and coalescence of earlier normal slip features and formation of most of the fractures and faults seen today (Aubert, 2020). The fault damage zone is composed mainly of two fracture sets striking N60E and N20W, but local variation in direction is observed depending on fault surface curvature (tortuosity) (see details in Aubert, 2020). Background barren opening-mode fractures (i.e. joints) pre-date normal movement in the Castellás fault zone, as evidenced by crosscutting relationships. These fractures regionally strike N30E and N60W, although locally a 10-degree departure from the regional strike is common (Aubert, 2020; Lamarche et al., 2012).

Petrographic analysis reveals a complex diagenetic history that involves several cementation stages as well as dissolution (Aubert et al., 2019, 2020). Diagenesis in the form of cement accumulation affected the host rock and faulted rock differently. The host rocks contain several phases of calcite filling primary and/or secondary porosity and most grains show some degree of micritization. Host rocks still preserve considerable porosity (mean = 15% porosity) at locations at least 20 m away from the main fault plane (Aubert et al., 2020).

Fractures within the Castellás fault zone also show evidence for multiphase calcite cementation (Aubert et al., 2019, 2020). Extensive calcite cementation within the fault zone resulted in low porosity (mean = 4.8%) relative to rocks distant from the fault (mean = 15%) and completely occluded fractures (Aubert et al., 2020). Oxides observed in

some fractures and in BR2 suggest that, despite overall low porosity, permeable conduits allowed water to percolate, depositing oxides into the fault zone, probably during the Pyrenean reactivation phase (Aubert, 2020). The lower porosity of the fault zone made it more weathering-resistant than the host rock surrounding it, giving place to high outcropping, continuous exposures of the fault core today (Fig. 2e).

Preferential cementation of the fault zone was probably caused by high-permeability, localized pathways that conducted cementing fluids close to the fault (e.g. Billi et al., 2003), but overall, the Castellás fault is thought to have a mixed behavior as either fluid conduit or barrier depending on local aspects like width of fault core, degree of cementation, local fault throw and facies variation (Matonti et al., 2012; Aubert et al., 2021). Our study builds upon the paragenetic sequence previously established by Léonide et al. (2014), Aubert et al. (2020) and Cochard et al. (2021) focusing on the absolute timing and effect of deformation and/or cementation on fault zone permeability.

3. Methods

To unravel the distribution and timing of diagenetic and deformation phases affecting the fault rocks we combined field data collection (fracture size, spatial distribution) with laboratory analyses (petrography, C and O stable isotope geochemistry and U–Pb geochronology).

3.1. Scanline acquisition

The size and narrow shape of the exposures mandated one-dimensional scanline data acquisition. Scanline data were acquired along a line oblique to the Castellás fault strike (Fig. 1b and c) with mean orientation N15E, as permitted by outcrop conditions. As scanline direction was oblique to the fracture set directions and fault (~60°), we used Terzaghi correction to obtain real spacings. We measured position along scanline, orientation, feature type (e.g. barren opening-mode fractures, cement-filled opening-mode fractures and fault) and kinematic aperture (opening displacement) for all structures that crossed the scanline trace. We use the term barren opening-mode fractures for

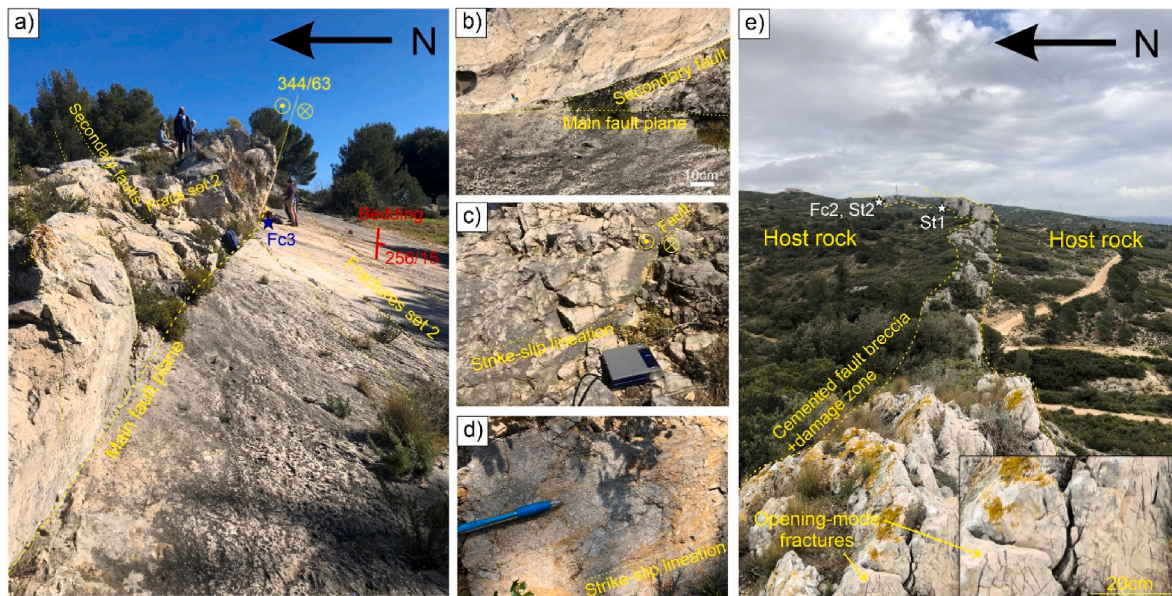


Fig. 2. Outcrop images showing fault, fractures, and diagenetic characteristics. a) Main fault plane, secondary fault planes and Set 2 fractures. Sample Fc3 location is shown in blue. Bedding orientation is shown in red. Orientation convention is dip azimuth/dip angle. b) Crosscutting relations showing abutting of secondary fault planes into the main fault plane. c) Sub-horizontal lineation showing strike-slip kinematics. d) Strike-slip lineation in the fault breccia (sample Fc3). e) Panoramic view of the Castellás fault zone. The hills in the center of the image (countered in yellow) are formed by cemented fault breccia and fractured damage zone. Calcite-filled opening-mode fractures can be observed on the bottom of the image. Inset shows detail of calcite-filled opening-mode fractures. Lateral low-relief areas are formed by porous host rock. Position of sample transects St1 and St2, and fault core sample Fc2 are shown in white. (For interpretation of the references to color in this figure legend, the reader is referred to the Web version of this article.)

fractures without cement fill (joints), and cement-filled opening-mode fractures for fractures filled with cement (veins). We prefer this terminology since it gives information about the type of filling and the fracture kinematics. In rare exceptions where weathering did not allow a reliable aperture measurement the presence of the fracture was recorded without an associated size value. Position was recorded using a measuring tape and by noting the exact position where the fracture crossed the scanline. In some parts of the outcrop, extrapolation of fracture traces to the scanline trace over short distances of less than a meter was used where visibility of the feature directly on the scanline trace was poor, a standard practice (e.g., Wang et al., 2019). Aperture was measured using a logarithmic graduated comparator rule (Ortega et al., 2006) and a 10 × hand-lens. Orientation was recorded using a dip azimuth/dip angle convention and the software Fieldmove Clino in an Iphone 8 mobile phone.

3.2. Structural analysis

We analyzed structural data from scanlines using a combination of cross-plots, stereonet projections, rose diagrams, and histograms (Figs. 3–5). For analysis we used software including DAISY 4.96.5 (Structural Data Integrated System Analyser; Salvini et al., 1999), Python 3.0 Jupyter notebook scripts and MSOffice Excel 2012.

For visual inspection of fracture spatial distribution, we used stick plots (Fig. 4a–c). We plotted dip angle and aperture along the scanline to

observe variations in these parameters along the scanline trace (Fig. 4d and e). Fractures striking more than 20° away from the mean azimuth of the identified fracture sets were not plotted, as a conservative way to analyze fracture sets individually.

We used the cumulative number of features to determine damage zone width (Choi et al., 2016). The curve is built by cumulatively counting the number of features along the scanline trace, starting at the fault plane position, and going towards the scanline limits (i.e., away from the fault plane and towards both starting and ending positions). We corrected the cumulative curve in intervals where data are abruptly missing (e.g., covered) to maintain a continuous slope, according to the method by Choi et al. (2016) (Fig. 4g). We created histograms using the GeostatsPy package (Pyrzcz, 2020) within a Python script to analyze fracture aperture distributions (Fig. 5).

3.3. Spatial arrangement

We analyzed the variation in spatial arrangement of fractures (i.e. distribution) using coefficient of variation (Cv) of spacings (Gillespie et al., 1993) and the normalized correlation count method (Laubach et al., 2018; Marrett et al., 2018). Cv is defined as the ratio of standard deviation to the mean of the spacings. Cv = 0 relates to perfectly periodic fractures, Cv = 1 for a random distribution, Cv > 1 for irregularly spaced fractures and Cv < 1 for regularly spaced (anticlustered) fractures (Gillespie et al., 1993). To allow analysis of Cv along the scanline

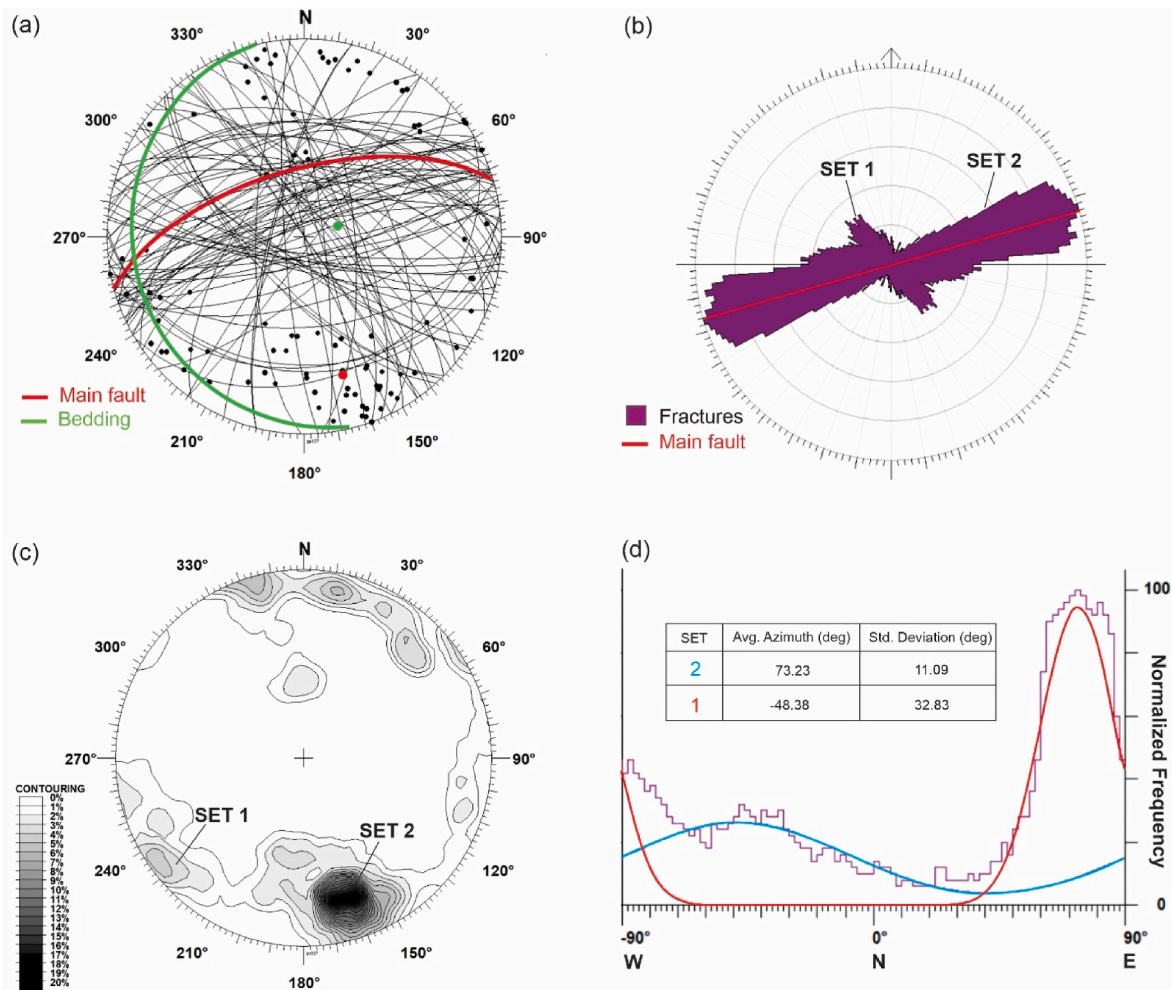


Fig. 3. Fracture orientation data as recorded along SL. (a) Lower hemisphere Schmidt net projections showing planes and poles to planes of fractures, main fault plane and bedding. (b) Smoothed rose diagram and main fault plane strike direction (1 smoothing interaction on 15% interval of data). (c) Stereonet with density contours (1%). (d) Strike histograms and best fit gaussian function parameters that indicate predominant trends of measured fracture orientations.

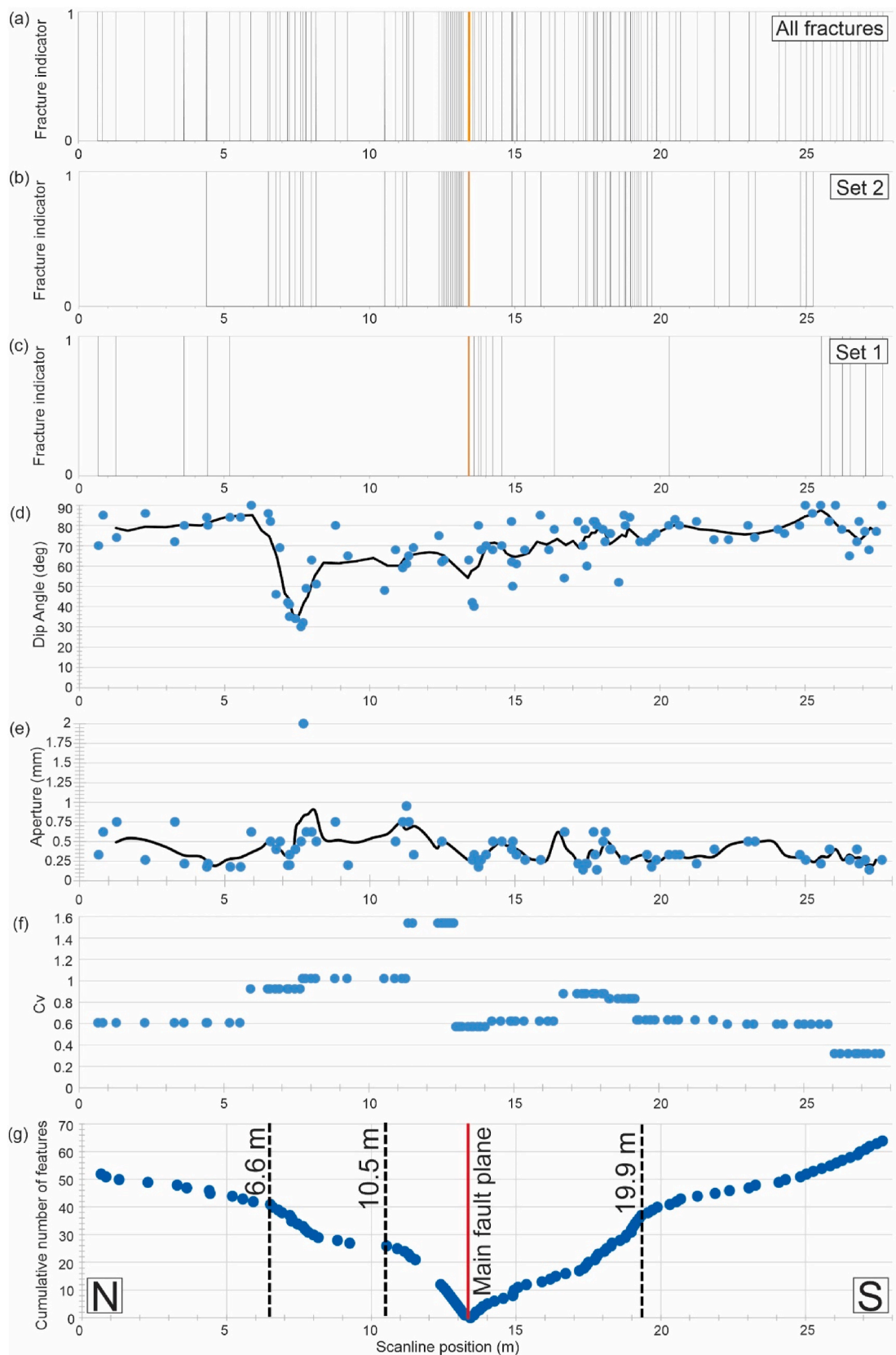


Fig. 4. Structural data measured along scanline trace. (a) Stick plot of all measured fracture positions. Yellow line shows the main fault plane position. (b) Filtered stick plot showing Set 2 fracture positions. (c) Filtered stick plot showing Set 1 fracture positions. (d) Fracture dip angle and moving average (black line) using interval of 5 samples. (e) Fracture aperture and moving average (black line) using interval of 5 samples. (f) Coefficient of variation of spacings using interval of 10 samples. (g) Cumulative number of fractures along scanline trace. The major slope changes marked can be interpreted as the limits of structural domains in the fault zone. North and South directions indicated. (For interpretation of the references to color in this figure legend, the reader is referred to the Web version of this article.)

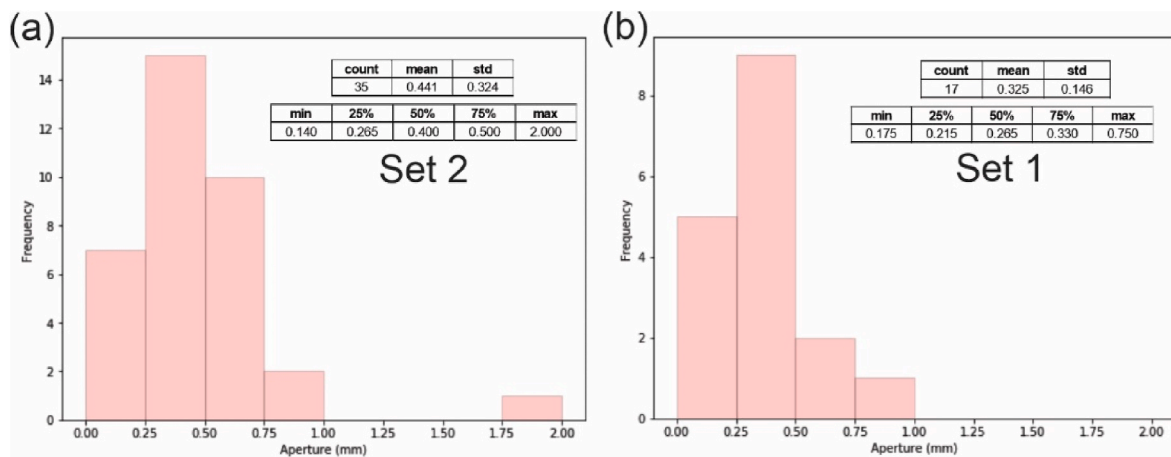


Fig. 5. Aperture size histograms and statistics (mean, standard deviation, minimum, maximum and intermediate quantile values) per fracture set.

we calculated Cv in windows of 10 increments along the scanline length (Fig. 4f).

A limitation of Cv is insensitivity to fracture sequence. Methods that account for inter-fracture distances and position provide a more nuanced view (e.g. Laubach et al., 2018; Marrett et al., 2018; Li et al., 2018; Sanderson and Peacock, 2019; Bistacchi et al., 2020; Wang et al., 2019). To further assess spatial arrangement, we relied on the Normalized Correlation Count (NCC) and associated freely available open-access software *CorrCount* (Marrett et al., 2018) (Fig. 6). The NCC method is based on the two-point correlation function (Hentschel and Procaccia, 1983; Bour et al., 2002; Du Bernard et al., 2002; Marrett et al., 2018). The NCC algorithm essentially compares the frequency of fracture distances in the input data with the expected value obtained from randomizations. Fractures are clustered if distances among fractures are more frequent than random, and anticlustered (or possibly regular) if distances are less frequent than random.

3.4. Petrographic and isotopic analysis

We collected 23 hand samples from seven locations along the Castellas fault zone (Fig. 1b). Sample Sdz (refer to Fig. 1 for sample names and locations) was recovered from the scanline trace in the damage zone on the southern side of the fault zone. The other samples are not on the scanline and include tectonic breccias from the fault core (Fc1, Fc2, Fc3), damage zone and host rock sampling transects (St1, St2, St3) (i.e. transects composed of several samples in similar locations) (Figs. 1b and 2a, e).

We analyzed relative cement chronology, composition and texture using conventional transmitted light optical microscopy, optical cathodoluminescence (CL), and C and O stable isotopic compositions. We conducted the petrographic analysis on a Zeiss Axio 40 microscope coupled to a Canon digital camera at the Department of Geosciences Microscopy laboratory at The University of Texas at Austin. We observed 27 thin sections in total, 3 from the fault core breccia and 24 from the damage zone with intact host rock. We acquired optical-CL using an Olympus BX43 microscope coupled to a Reliotron cathodoluminescence instrument and an Olympus DP73 digital camera at the Department of Geosciences Electron Micro Beam facility at the University of Texas at Austin. We used 8–9 kV of beam voltage and 100 μ A–300 μ A of beam current under vacuum.

We analyzed C and O stable isotopic compositions at The University of Texas at Austin, Bureau of Economic Geology stable isotope laboratory using rock powders that were collected with a Dremel 100 micro-drill from six cement locations (four distinct cement phases) in samples Sdz and Fc3. We drilled and collected each cement phase separately in individual plastic vials for analysis. In between each sample collection,

the drill was cleaned using a solution of water and alcohol. Aliquots of \sim 0.3 mg were analyzed for $\delta^{13}\text{C}$ and $\delta^{18}\text{O}$ using a Thermo Fisher Scientific GasBench II coupled to a Thermo Fisher Scientific MAT 253 Isotope Ratio Mass Spectrometer (R ev esz and Landwehr, 2002; Sp otl and Vennemann, 2003). Samples were reacted in helium-flushed vials with 103% H_3PO_4 at 50 $^\circ\text{C}$ for 8 h. Data were calibrated using calcite standards NBS-18 ($\delta^{18}\text{O}_{\text{VPDB}} = -2.3\text{‰}$, $\delta^{13}\text{C}_{\text{VPDB}} = -5.0\text{‰}$) and NBS-19 ($\delta^{18}\text{O}_{\text{VPDB}} = -2.3\text{‰}$, $\delta^{13}\text{C}_{\text{VPDB}} = 1.95\text{‰}$). Replicates of an internal carbonate standard were analyzed throughout the analytical session to account for analytical drift and precision, reaching an analytical precision of $\pm 0.06\text{‰}$ for $\delta^{13}\text{C}_{\text{VPDB}}$ and $\pm 0.10\text{‰}$ for $\delta^{18}\text{O}_{\text{VPDB}}$ routinely. Values are reported in ‰VPDB .

3.5. LA-ICP-MS U–Pb geochronology

Calcite U–Pb geochronology was conducted at the UTChron laboratory at The University of Texas at Austin. The laser ablation inductively coupled plasma mass spectrometry (LA-ICP-MS) system consisted of a Photon Machines Analyte G2 ArF excimer 193 nm laser, equipped with a two-volume Helix sample cell, coupled to a Thermo Element 2 double-focusing magnetic sector ICP-MS. Helium was used as the carrier gas and mixed with Argon before entering the ICP-MS. The analyses were conducted on polished rock billets (samples Fc3 and Sdz) and thin sections (samples Fc1 and Fc2) in static spot mode with a laser beam diameter of 110 μm , operated with an energy density of 4.08 J/cm² measured with an energy meter, and a pulse rate of 10 Hz. Each analysis consisted of 4 cleaning shots, 27 s of baseline data collection, 30 s of ablation and 27 s of washout.

Elemental and isotopic fractionation were corrected by interspersed analysis of primary calcite reference material WC-1 (206 Pb/238U 254.6 \pm 6.4 Ma; Roberts et al., 2017). Analyses were made in repeating blocks of two standards, followed by ten unknowns, with NIST614 measured periodically to monitor Pb isotopic fractionation. Age calculation was performed using Iolite v3.7 (Paton et al., 2011) and VizualAge UcomPbine (Chew et al., 2014). A ²⁰⁷Pb common Pb correction was applied to correct for common Pb in the primary reference material (WC-1 ²⁰⁷Pb/²⁰⁶Pb = 0.85).

Between 8 and 42 spots were analyzed on each region of interest (fracture cement, host rock primary pore cement, host rock matrix grain). Time-integrated data were exported as entire 30 s ablation windows if isotopically homogenous or broken up into 2–4 shorter ablation windows if exhibiting isotopic variation. U–Pb data were plotted on Tera-Wasserburg diagrams and lower intercept ages calculated using IsoplotR (Vermeesch, 2018). Errors for isotopic ratios and ages are presented as 2-sigma absolute errors (2 σ) (see Appendix for metadata of the LA-ICP-MS analysis).

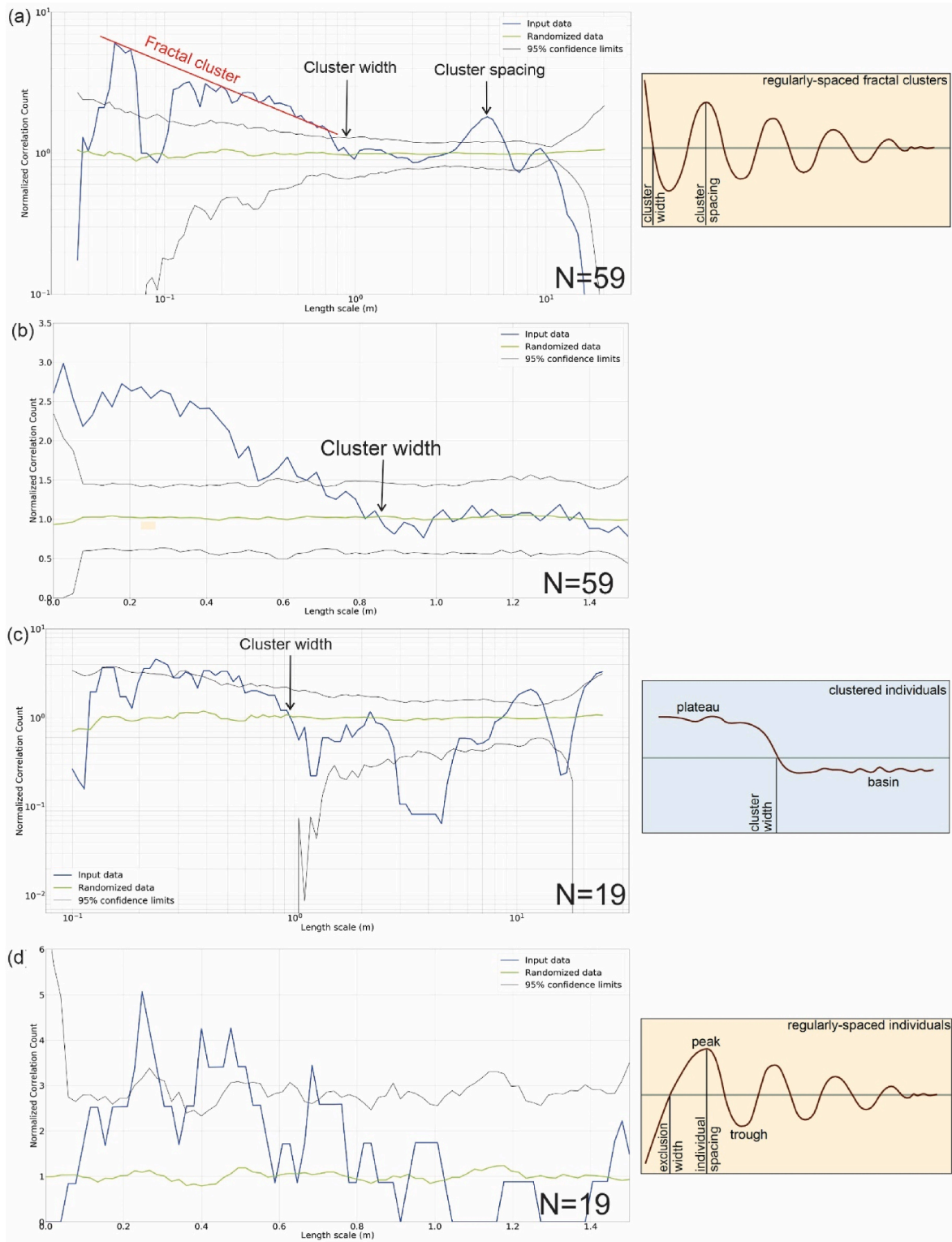


Fig. 6. Spatial arrangement analysis using NCC. For length scales where $NCC > 1$, fracture spacings are more frequent than random. For length scales where $NCC < 1$, fracture spacings are less frequent random. Resulting graphs use approximately 100 length scale samples, a smoothing window of 2 and 100 Monte Carlo simulations. Yellow and blue boxes, on the right, show correspondent ideal NCC pattern for each type of spatial arrangement observed, see Marrett et al. (2018) for pattern interpretation. (a) Set 2 NCC plot using logarithmic scale ($N = 59$). Cluster width and cluster spacings are indicated on the plot. Red line shows the behavior of fractal clusters on the logarithmic plot. Yellow inlet shows the ideal behavior of fractal clusters in NCC. (b) Set 2 normalized correlation count plot using linear scale, showing length scales below cluster width. Smaller length scales are increasingly more clustered than longer length scales, which is a fractal characteristic. (c) Set 1 normalized correlation count plot using logarithmic scale ($N = 19$). Cluster width is indicated. Blue inlet shows the ideal pattern of NCC curve forming a plateau, in the case of clustered individuals. (d) Set 1 normalized correlation plot for small length scales (< 1.5 m) using linear scale. Yellow inlet shows the ideal NCC pattern of regularly spaced fractures, which is coherent with what was observed in our data. (For interpretation of the references to color in this figure legend, the reader is referred to the Web version of this article.)

4. Results

4.1. Structural characterization

The main fault plane strikes N77E, dips 63° to the NW and shows strike-slip striations (Fig. 2c and d). A few secondary slip planes locally strike E-NE (Fig. 2a and b). Beds dip ~15° to the SW. Structural features

near the fault plane are predominantly at high angles to bedding. Most fractures strike in two main orientations, N48W (Set 1) and N73E (Set 2, parallel to the main fault plane), and dip steeply (mean = 70°; stdev = 13.6°) (Fig. 3). Both Set 1 and Set 2 fractures are calcite-filled opening-mode fractures. Set 2 fractures terminate against horizontal stylolites (Fig. 7e), as crosscutting shows. The strike dispersion around the mean azimuth of Set 1 (stdev = 32°) suggests that other fracture sets (with

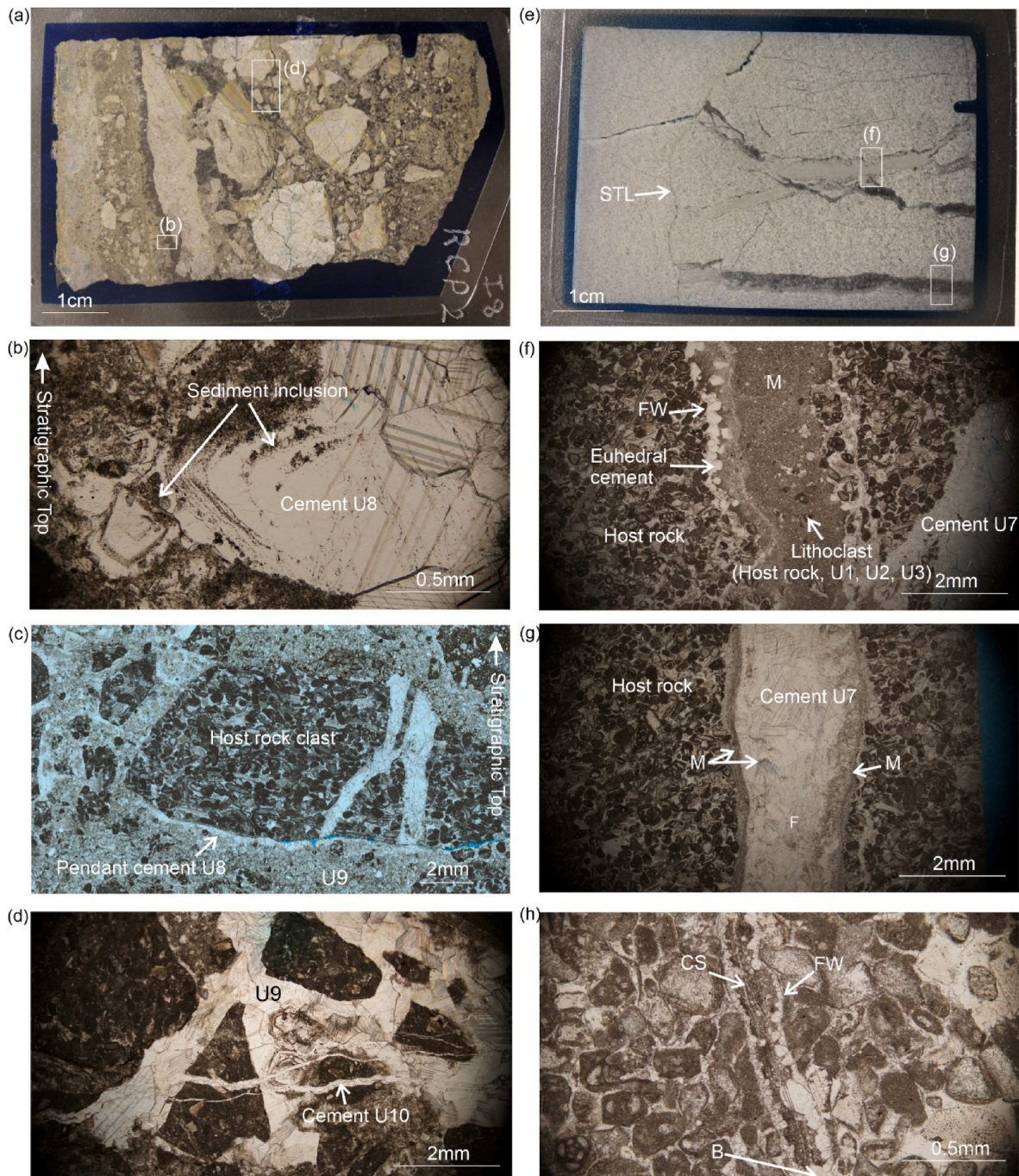


Fig. 7. Transmitted light photomicrographs from sample Fc3 (a,b,d), damage zone sample Sdz (e–h), and sample Fc1 (c). (a) Thin section of sample Fc3 showing BR2 and position of detailed images. (b) Dogtooth calcite cement U8 showing asymmetric sediment inclusions (PPL) in direction to stratigraphic top as indicated. (c) Calcite cement U9 filling BR2 intraclast porosity (PPL) and pendant cement U8, deposited towards stratigraphic bottom. (d) BR2 cemented by U9 with calcite-filled opening-mode fractures cemented by U10 cross-cutting U9, and subrounded clasts of host rock (XPL). (e) Thin section of sample Sdz showing host rock and two fractures, one filled with micrite and the other with calcite cement. Some fractures end at stylolites (STL). (f) Set 2 calcite-filled opening-mode fracture with euhedral dogtooth cement lining fracture walls (FW) and micritic infill (M) with pieces of broken host rock containing U1, U2 and U3 (PPL). (g) Reactivated fracture (F) showing micritic infill (M) on the walls and calcite cement in the middle (PPL). (h) Calcite-filled opening-mode fracture showing both euhedral cement on fracture wall (FW), micritic infill and crack-seal texture (CS). Calcite cement bridge (B) is present on the lower part of the image (PPL).

discrete orientations) may be present in the area but could not be properly captured by our field structural data.

We measured 109 fractures along a 27.65 m-long scanline oriented obliquely to the main fault surface and Set 2 (Fig. 3d). The distribution of the measured Set 2 strike follows a N73E mean azimuth, but it is considerably skewed towards the E-W direction indicating the potential presence of another, undifferentiated fracture set. Based on the difficulty to further separate the data into subsets using strike data alone, we considered all NE fractures measured along this scanline to be part of Set 2.

We used the cumulative number of fractures to define damage zone width (Choi et al., 2016) (Fig. 4g). The main fault surface (plane) is at position 13.42 m along the scanline. We did not find fault core breccia along the scanline trace, but it outcrops in other locations (Fig. 2). The curve suggests that on the southern portion the damage zone (DZS) ends at position 19.9 m, yielding a 6.5 m-wide damage zone. On the northern portion, the curve shows two slope breaks, one at position 10.5 m and another at position 6.6 m. This suggests the presence of an inner (DZN1) and an outer (DZN2) damage zone, 2.9 m and 6.8 m wide respectively. We consider DZS and DZN2 to encompass the entire damage zone region, suggesting a symmetric damage zone around the Castellas fault in this location with a total width of 13.3 m.

Most Set 2 fractures are near or within the damage zone, whereas Set 1 is mostly evident outside of it (Fig. 4a,b,c). Inside the damage zone, fractures dip less steeply than outside of the damage zone (Fig. 4d). The shallowest fractures are in DZN1, reaching dips as low as 30°. In the undamaged host rock, fractures approximate vertical dips.

Fracture kinematic aperture sizes range from 0.14 mm to 2 mm, with larger apertures apparent in the damage zone (Fig. 4e). Set 2 has a wide aperture size range with apertures of as much as 2 mm and a mean aperture of 0.441 mm (stdev = 0.324 mm). Set 1 reaches a maximum aperture of 0.75 mm with a mean aperture of 0.325 mm (stdev = 0.146 mm) (Fig. 5).

4.2. Spatial arrangement

The coefficient of variation (Cv) (ratio of std. deviation to the mean of fracture spacings; see methods section) of the fracture data in the scanline provided essential information about the spatial arrangement of the fractures. The combined Cv for both fractures sets together is lower in the host rock (i.e. regular fracture spacing) and higher inside the damage zone (i.e. clustered fractured spacing) with increasing values towards the main fault surface, especially in the northern portion of the fault zone (Fig. 4f). Considering fractures in Set 1 and Set 2 separately, Cv = 1.56 for Set 1 and Cv = 2.01 for Set 2. However, large intervals within the damage zone lack Set 1 fractures. If this section is excluded from the analysis, Set 1 shows Cv = 0.61 in the host rock outside of the damage zone, which is consistent with this set's apparent regular spacing in outcrop and upon visual inspection of stick plots (Fig. 4c).

The NCC method provides another way to quantify the spatial arrangement of the fractures and showed markedly different patterns between sets. By comparing the NCC curve of scanline data with NCC curves of several idealized arrangements (Marrett et al., 2018) and randomizations, one can determine the spatial arrangement of the input data. Set 2 shows a statistically significant fractal cluster behavior (Fig. 6a and b). The NCC curve displayed on logarithmic scales crosses expected NCC value at 0.9 m, indicating fracture clusters are ~0.9 m in width and spaced at ~5 m (Fig. 6a, see Marrett et al., 2018 for a guide to interpretation of NCC patterns), suggesting that Set 2 fractures follow a regularly spaced fractal cluster pattern. For length scales smaller than the cluster width (0.9 m) the NCC curve shows increasing values towards small length scales (Fig. 6b), which is characteristic of fractal patterns (e.g. Dichiarante et al., 2020).

On a logarithmic scale, Set 1 shows a plateau-shaped curve for length scales <0.95 m, suggesting a clustered pattern with cluster widths of

0.95 m (Fig. 6c). For length scales <0.95 m, however, Set 1 fractures appear to be regularly spaced with an individual spacing of 0.24 m as indicated by the wavy pattern on the linear plot (Fig. 6d). As Set 1 mostly appears in the host rock, this spatial arrangement is influenced by the presence of an "exclusion zone" in the damage zone where Set 1 is absent. The regular spaced pattern observed for smaller scales appears to be less impacted by the exclusion zone and is probably indicative of the true arrangement of Set 1 fractures. Both analysis of Cv and NCC are coherent with each other and suggest a clustered behavior for Set 2, mostly present in the damage zone, and regular spacing for Set 1, mostly present in the host rock.

4.3. Petrography

The host rock is mostly Urganian micritized peloid foraminifera grainstone with smaller proportions of echinoderms and ooids (Fig. 7f and g). Most of the grains have been affected by early micritization that formed micritized rims around grains or affected the entirety of grains, hindering the identification of some of the original grain fabrics (e.g. Léonide et al., 2014; Aubert et al., 2020). The primary fabric of the host rock suggests a high initial porosity (c.a. 15%), because no primary micrite is identified, and the rock is exclusively grain-supported. We identified 11 calcite cement phases filling primary pores, fault breccias and calcite-filled opening-mode fractures (Table 1). Each phase is discriminated from each other by its distinct cathodoluminescence color, crystal habit, and where possible, cross-cutting relationships (e.g. Fig. 9b). Primary pores in host rock are filled with four early calcite cement phases (U1 – U4) (Fig. 8). Most host rock grains have an

Table 1

Characteristics of cement phases identified in this study compared to previous studies of similar rocks.

This study	Aubert et al. (2020)	Léonide et al., 2014	Cochard et al. (2021)	Characteristics	Location
U1	C0	S1	C1	Concentric bladed rim around grains, non-luminescent/purple	Host rock
U2	C1a	S2	C2a, C2b	Dog tooth, non-luminescent/purple	Host rock/ Fractures
U3	C1b			Zoned, granular, yellow bright luminescent	Host rock/ Fractures
U4	C3			Blocky, dull orange luminescence	Host rock/ Fractures
U5	C2		C3a, C3b	Blocky, dull red/orange luminescence, dark spots	Fractures
U6				Blocky, orange luminescence	Fractures
U7			C4a, C4b	Blocky, dull red luminescence	Fractures
U8				Dog tooth, dripstone, zoned, orange luminescence	Breccia
U9				Blocky, zoned, dull orange luminescence, sediment inclusions	Breccia
U10	C4a		C5	Blocky, non-luminescent	Fractures
U11	C4b			Blocky, zoned, yellow bright luminescent	Fractures

*Resulting cement phases from other studies in Urganian carbonates are shown for comparison.

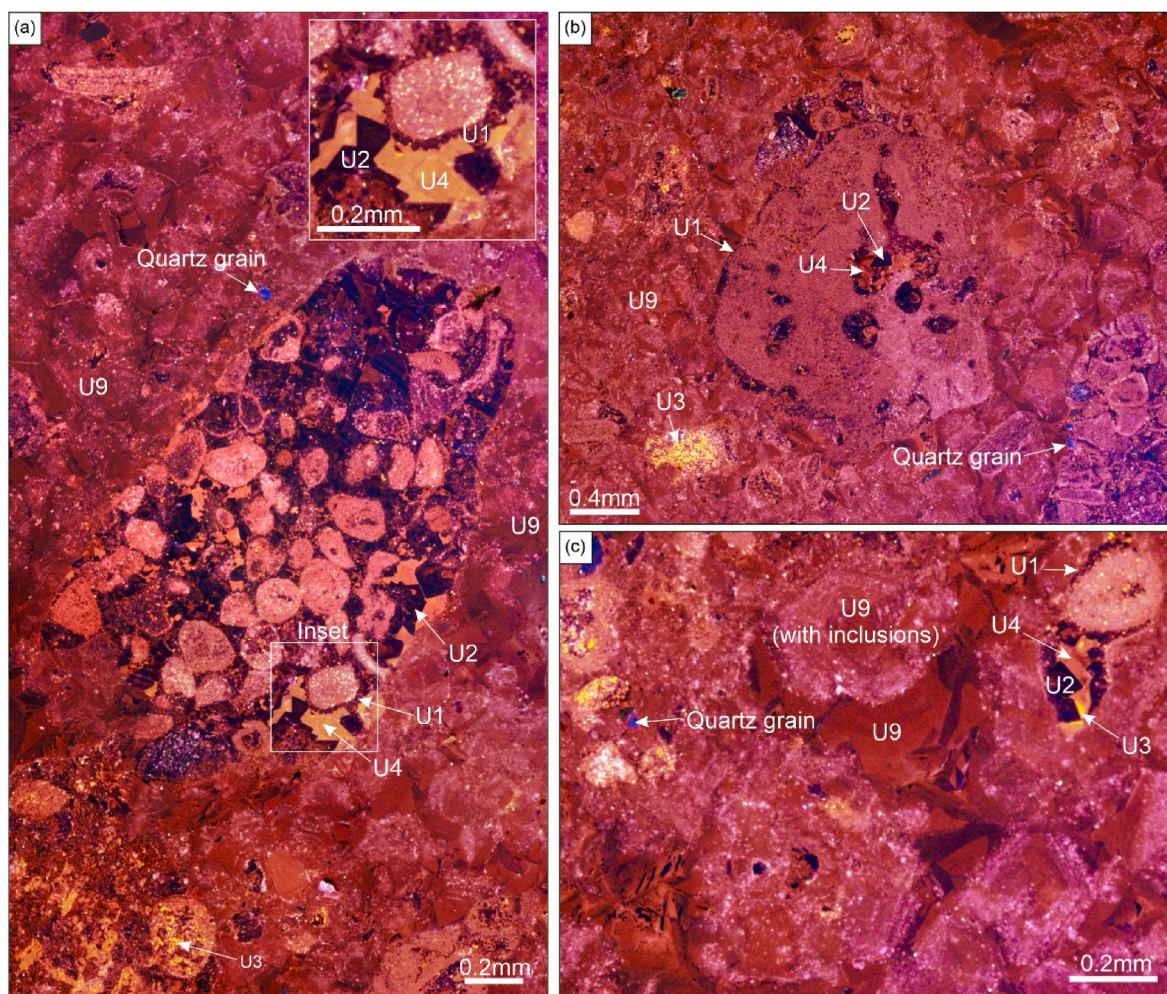


Fig. 8. Optical cathodoluminescence images of sample Fc2 showing host rock pore and breccia cements. (a) BR2 showing cement U9 and a host rock clast with primary pore cementation. Cement U9 shows sediment inclusions including quartz grains. Host rock clast shows primary pores filled by cement phases U1, U2, U3 and U4. Inset shows zoom into a primary pore with cement sequence U1, U2 and U4. (b) BR2 cemented by U9 showing cements U2, U3 and U4 filling secondary pores in a host rock clast. (c) Image of a host rock clast in BR2 showing the sequence of primary pore cement fill U1, U2, U3 and U4. Cement U9 can be observed with and without inclusions.

orange/red luminescence, whereas U1 and U2 cements are non-luminescent/purple-luminescent causing the host rock to show an overall dark tone under CL. Less abundant U3 is bright yellow-luminescent, and it is zoned where it fills primary pores, whereas U4 is dull orange-luminescent (Fig. 8).

Within the damage zone, sediment-filled and calcite-filled opening-mode fractures are common, mostly of Set 2 (Figs. 2 and 7e, f, g, h). We did not observe Set 1 fractures in thin section. Some Set 2 fractures have micritic linings and blocky calcite in the center (Fig. 7g). We identified several additional fracture categories not recognized in the field. Most notably, an older set of sediment-filled fractures with irregular walls, euhedral dog-tooth calcite cement linings, and sediment infill in the center that includes a mixture of micrite, lithoclasts – broken pieces of cemented host rock – fossils and cement fragments (Fig. 7f, h; Fig. 9a).

U2 cement linings in pores and fractures are characteristically non-luminescent and euhedral in shape facing pores (Figs. 8a and 9a, b, c). The micritic sediment infiltrated into fractures has a dull red luminescence, whereas lithoclasts within sediments that fill opening-mode fractures contain U2, U3 and U4 cement as indicated by their distinct luminescence (Fig. 9a).

Some sediment-filled fractures show crack seal texture (Ramsay, 1980; e.g., Ukar and Laubach, 2016) suggesting several re-cracking episodes and syn-kinematic cementation during active fracture

opening (Fig. 7h). Crack-seal texture is visible as thin (c.a. 50 μm) gap deposits within 0.4 mm-wide, sediment-filled opening-mode fractures (Fig. 7h). Some narrow fractures show isolated cement accumulations that span across the fracture forming cement bridges (Laubach et al., 2004) (Fig. 7h). Calcite bridges are absent in wide fractures.

The intensely deformed fault core is mostly composed of BR2 breccia, which shows a clast-supported fabric (Gs-type breccia of Ferraro et al., 2018) or mosaic breccia (Woodcock and Mort, 2008; e.g., Billi, 2010) (Fig. 7a), with an observed thickness of at least 30 cm at Fc3 location (Fig. 7a). BR2 clasts are angular to rounded of at least four types: Lithoclastic wackestone, peloid foraminifera grainstone, sandy limestone, and BR1 carbonate breccia (Fig. 7a; Fig. 9b). Most clasts in sample Fc3 are wackestones or carbonate breccias, whereas in Fc1 and Fc2 the clasts are mostly grainstones with one occurrence of sandy limestone. BR2 appears intermittently along the main fault plane, with varying thickness (Matonti et al., 2012). Textures and cross-cutting relationships pertaining to pre-BR2 can be observed within some BR2 clasts (Fig. 9b).

Observation in thin section helped to establish the following chronological sequence of cements in fractures and pores (Table 1):

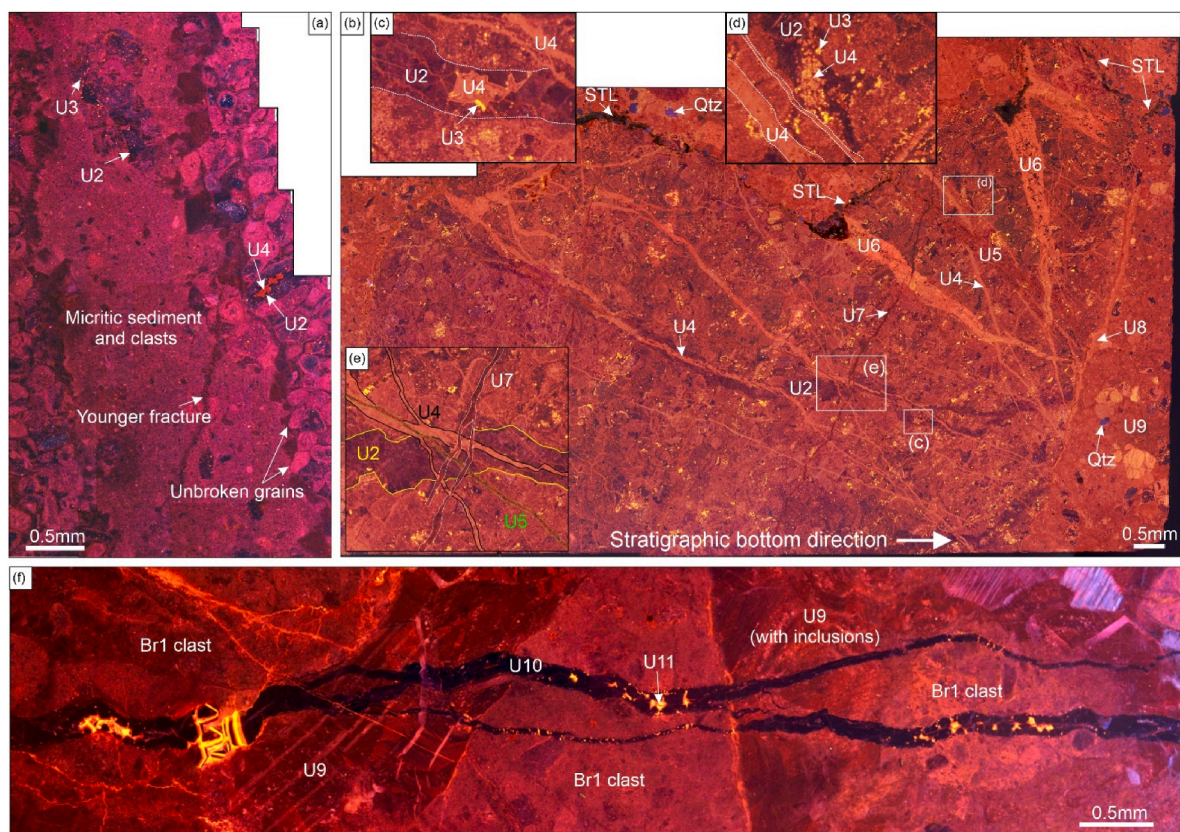


Fig. 9. Optical cathodoluminescence image of calcite-filled opening-mode fractures and fault breccia. (a) Calcite-filled opening-mode fracture with euhedral cement lining fracture walls (Sample Sdz). Fracture walls have unbroken grains. Micritic sediment infill showing host rock lithoclasts cemented by U2 and U3. (b) Fractured host rock clast (sample Fc1) showing several generations of calcite-filled opening-mode fractures and cross-cutting relationships. Stylolite (STL) contours the clast and concentrates quartz grains (QTZ) around it. Cement U8 is deposited around clasts only towards stratigraphic bottom. Cement U9 fills breccia porosity with infiltrated quartz grains. (c) Detail of oldest fracture observed in this clast, mostly filled with U2, but showing the same cement fill sequence U2, U3 and U4 as observed in primary pores (see Fig. 8 for more primary pore cements). (d) Primary pore showing cement fill and calcite-filled opening-mode fracture filled by cement U4. (e) Zoom of the cross-cutting relationships between fractures filled with cement sequence U2, U4, U5 and U7. (f) Calcite-filled opening-mode fracture filled by cement U10 and U11 cross-cutting cement U9 and clasts within BR2 (Sample Fc3).

- 1) First phase of non-luminescent cement U1, not observed in fractures, fills primary pores creating a bladed rim around host rock grains (Fig. 8a - inset).
- 2) Non-luminescent U2 cement fills the oldest fracture observed in sample Fc1 (Fig. 9c) and primary pores (Fig. 8a - inset, Fig. 8c).
- 3) U3 and U4 cements fill remaining host rock and fracture pore space (Fig. 9c), confirming the same relative chronological order (U1 to U4) in both features (Fig. 8a). U4-filled fractures can be observed crosscutting U2-filled fractures (Fig. 9b).
- 4) Several younger phases of cement, that are exclusive to calcite-filled opening-mode fractures, can be observed crosscutting each other in BR2 (Fig. 9), including a dull red/orange-luminescent calcite cement with dark inclusions (U5), an orange-luminescent calcite (U6), and a dull red-luminescent cement (U7), which is the last pre-BR2 cement phase observed. We used mutual cross-cutting relationships for U2–U4–U5–U7 to establish their relative chronology (Fig. 9e).
- 5) We observed a thick pendant, orange-luminescent calcite cement rim (U8) deposited only towards stratigraphic bottom around clasts within BR2 (Figs. 7c and 9b). Some parts of U8 crystals have sediment inclusions (Fig. 7b), indicating that sediment was infiltrating from the stratigraphic top and depositing on the calcite crystal as it grew into pore space. In some parts, BR2 show interstitial sediment deposits and oxide rims around U8.
- 6) Most of the remaining inter-breccia clast porosity was filled by a dull orange-luminescent blocky calcite (U9), also commonly bearing sediments, including quartz grain inclusions (Figs. 7d and 9b).
- 7) Younger, calcite-filled opening-mode fractures cut interstitial cements and clasts within BR2, and are filled by both a non-luminescent (U10) and a last phase of cementation formed by a bright yellow-luminescent cement (U11) (Fig. 7d; Fig. 9f), which is the last cement phase observed in all the samples.

Although many of the cement phases had several solid sediment inclusions, we did not observe in any of them large fluid inclusions suitable for microthermometry.

4.4. Geochemistry

We obtained a total of six rock powders for stable isotopic analyses of cement phases U2, U7, U9 and U10 (Fig. 10). Cement U2 have $\delta^{13}\text{C}$ 0.64‰ and $\delta^{18}\text{O}$ –6.91‰. Cement U7 have $\delta^{13}\text{C}$ values 1.32‰ and 0.82‰ and $\delta^{18}\text{O}$ values –6.26‰ and –6.76‰. Cements U9 and U10 have lower $\delta^{13}\text{C}$ than observed for U2 and U7 cements, but show overlap in $\delta^{18}\text{O}$ values. U9 preserves $\delta^{18}\text{O}$ –6.44‰, that is similar to U2 and U7, but lower $\delta^{13}\text{C}$ at –0.22‰. U10 is markedly different from the other samples with $\delta^{13}\text{C}$ values –2.07‰ and –1.53‰, and $\delta^{18}\text{O}$ values –7.18‰ and –4.65‰ (Table 2).

4.5. U–Pb geochronology

We dated calcite cements in four samples (Fig. 11). Features that were large enough for dating using a 110 μm laser size were the host

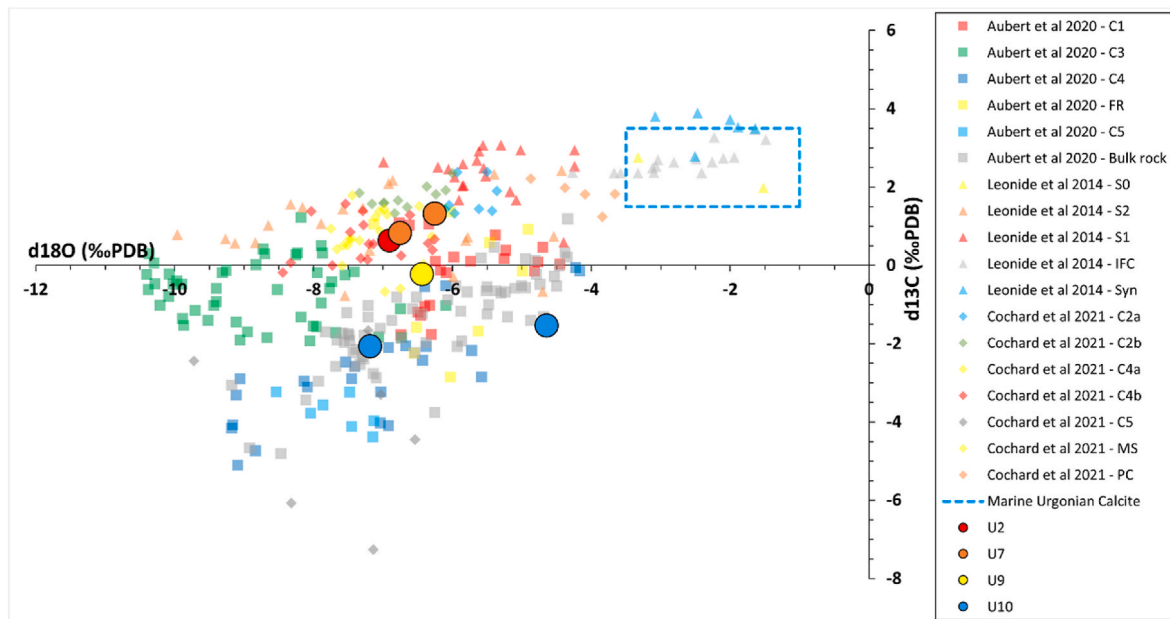


Fig. 10. Cross-plot of isotopic ratios ($\delta^{18}\text{O}$ versus $\delta^{13}\text{C}$) showing data from this study (solid circles) and from previous studies (transparent symbols and boxes). Dashed rectangle show isotopic ratios of marine Urgonian calcites from Moss and Tucker (1995).

Table 2
 $\delta^{13}\text{C}$ and $\delta^{18}\text{O}$ stable isotope composition of cement phases.

Sample	Cement phase	$\delta^{13}\text{C}$ (‰ VPDB)	$\delta^{18}\text{O}$ (‰ VPDB)
Fc3	U9	-0.22	-6.44
	U10	-2.07	-7.18
Sdz	U2	0.64	-6.91
	U7	1.32	-6.26
	U7	0.82	-6.76
	U10	-1.53	-4.65

rock, micritic sediment fill, U2, U6, U7, U8, U9, and U10 cements (Fig. 12, Table 3). Ages of host rock grains and U2 cement in host rock primary pores and in fractures vary between 103.8 Ma and 82.4 Ma. Micritic infill and U6–U10 cements in fractures and breccias (they are absent in primary pores) are younger, with ages between 52.8 Ma to 39.8 Ma. We did not find large crystals of cements U3, U4 and U5 big enough to fit the laser ablation spots (110 μm each) in any sample, and thus these cement phases were not dated.

5. Discussion

5.1. Timing of fracturing in relation to the castellas fault

Set 1 calcite-filled opening-mode fractures are nearly absent within the fault damage zone suggesting formation of this set is unrelated to the main fault activity. The strike and bed-perpendicular dip of Set 1 fractures are compatible with early, vertical burial-related fracturing described regionally in Urgonian carbonates (please see Lamarche et al., 2012 for an expanded discussion). Moreover, the regular spacing of Set 1 (Low Cv; Fig. 4c,f; Fig. 6d) was likely controlled by bed interfaces (e.g. Rives et al., 1992; Bao et al., 2019; Chemenda et al., 2021), further indicating that this is a pre-Castellas fault, regional fracture set. By contrast, Set 2 calcite-filled opening-mode fractures follow the same orientation as the main fault, have larger kinematic apertures (Fig. 5), are mostly present within the damage zone and are highly clustered, with ~ 0.9 m-wide clusters regularly spaced every 5 m around the main fault (Fig. 4e and f; Fig. 6), providing strong evidence that genesis of Set 2 fractures is related to the Castellas fault. Set 1 and Set 2 are equally

oblique to the scanline direction ($\sim 60^\circ$), meaning that the scanline was able to detect both fracture sets with apparent spacings due to misorientation. However, as they are equally misoriented with respect to scanline direction, none of the sets were disproportionately affected by this issue. We used Terzaghi corrected spacings to assess fracture sets spatial arrangement, allowing us to analyze their properties correctly.

We identified eleven generations of cements (U1–U11) within Set 2 calcite-filled opening-mode fractures (Table 1). This newly established sequence correlates with previous works (Aubert et al., 2020; Aubert, 2020) and adds a few stages that were previously unidentified. The relative chronology established based on cross-cutting relationships (section 4.3) combined with direct U–Pb dating of calcite provides a solid interpretation of the sequence of cementation (Table 1) and allows establishing a link with regional tectonic events. Host rock grains ages (91 ± 24.2 Ma and 82.4 ± 21.2 Ma) are contemporaneous with the Albian-Cenomanian Durancian uplift event (e.g. Guyonnet-Benaize et al., 2010), which is younger than the estimated Barremian deposition age of Urgonian carbonates (125 Ma) (Aubert et al., 2019; Godeau et al., 2018). The younger age and large uncertainty (2-sigma) obtained for host rock grains is likely related to the widespread micritization of grains that could have affected U/Pb ratios.

The minimum age of U2 cement in fractures (87.2 ± 7.2 Ma) and in intergranular host rock pore space (103.8 ± 15.0 Ma) also indicates precipitation during the Durancian uplift (Fig. 9a and b). Ages are consistent with what was obtained by Godeau et al. (2018) (92.4 ± 1.7 Ma). The fact that U2-bearing fracture walls contour host rock grains indicates that the host rock was under-consolidated during initial brittle deformation (Fig. 9a). This indicates a very early fracturing phase during the Durancian uplift, when the Castellas fault had a normal-slip phase (Matonti et al., 2012). Although U3–U4 cements were not large enough to be dated, the presence of U2 through U4 in both primary pores (Fig. 8c) and old fractures (Fig. 9c), suggests contemporaneous cementation of the host rock and fractures during the Late Cretaceous.

Despite large 2-sigma uncertainties, U6 to U10 cements showed younger ages (52.8 ± 10.7 Ma to 39.8 ± 8.1 Ma) indicating cementation during the Eocene Pyrenean orogeny (e.g. Guyonnet-Benaize et al., 2010; Parizot et al., 2021) when the Castellas fault was reactivated in strike-slip movement (Matonti et al., 2012). U6 and U7 are part of a subgroup of cements filling only fractures, while U8 through U10 are

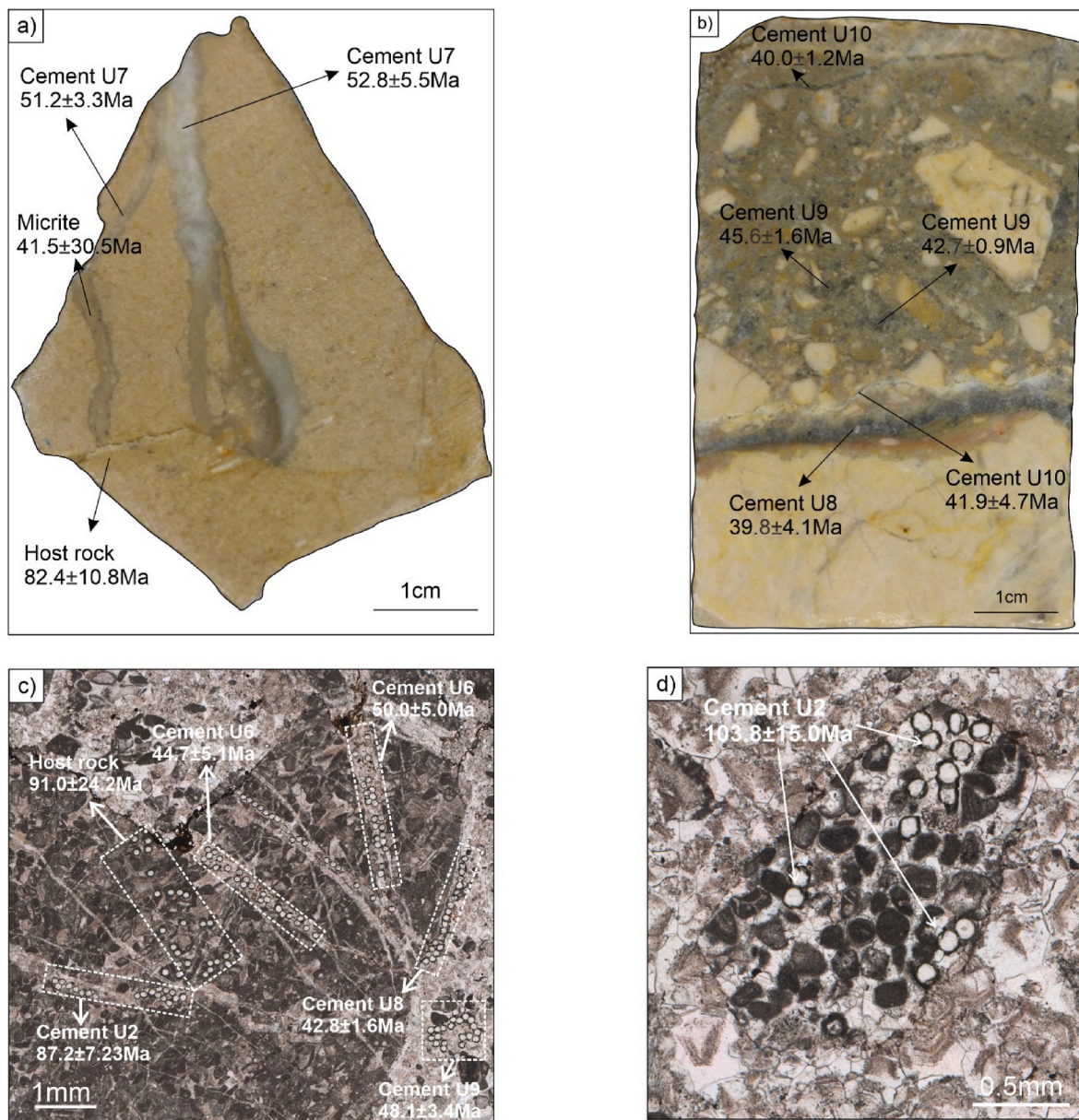


Fig. 11. Laser-ablation spots and calcite U–Pb ages acquired from calcite-filled opening-mode fractures, breccia and host rock cements in billets and thin sections. a) Damage zone sample (Sdz). b) Fault breccia sample (Fc3). c) Fault breccia sample (Fc1) (Refer to Fig. 8b for an image taken before laser ablation). d) Fault breccia sample (Fc2) (Refer to Fig. 7a for an image taken before laser ablation).

later and especially U8 and U9 are related to the creation of BR2 fault breccia, when deformation was more intense. None of these cements are present in the host rock, indicating that the host rock was thoroughly cemented in the Late Cretaceous. Our samples did not yield any ages younger than Eocene, which is consistent with most Set 2 calcite-filled opening-mode fractures forming and becoming cemented prior to the Miocene Alpine orogeny.

Important variables that impact the quality of the U–Pb ages are the relative amounts of common-lead to radiogenic U and Pb isotopes and the count rate, which can be seen affecting the values of 2-sigma age uncertainty in our dataset. Calcite is a common-lead-bearing mineral and usually shows very low amounts of Uranium (ca. 10 ppb to 10 ppm) (Roberts et al., 2020). Due to this, the Tera-Wasserburg diagrams (see Appendix) show a high common-lead composition, meaning that most data points are located on the upper left corner of the diagram, with limited amounts of higher uranium calcites used to anchor the isochron's lower intercept on concordia curve. Ages obtained with this kind

of data can have high 2-sigma errors, such as above 8My, like observed for the host rock (Fc1 and Sdz), micrite (Sdz) and cements U7 (Sdz), U8 (Fc3) and U10 (Fc3). The very high 2-sigma uncertainty of the micrite age (30.5 My), is also caused by the predominance of common-lead, and means that this data must be used with care. The count rate defines the size of the error ellipse, and thus also have an impact on the isochron regression. Low count rates will cause larger error ellipses and will increase the lower intercept age uncertainty. This effect can be seen mostly affecting cement U7, which shows high 2-sigma errors (6.4 and 10.7 My) and big error ellipses. In other cases, we obtained good isochron ages with lower 2-sigma errors around 2My, such as for cements U9 (Fc3), U8 (Fc1) and U10 (Fc3), due to a good mix of common-lead and radiogenic isotopic composition.

A key premise to using calcite cement to date faults or fractures is that cementation occurred during (syn-tectonic) or shortly after fracturing. Crack-seal textures and slickenfibers are the most reliable structures indicative of syn-tectonic fracturing and/or faulting (e.g.

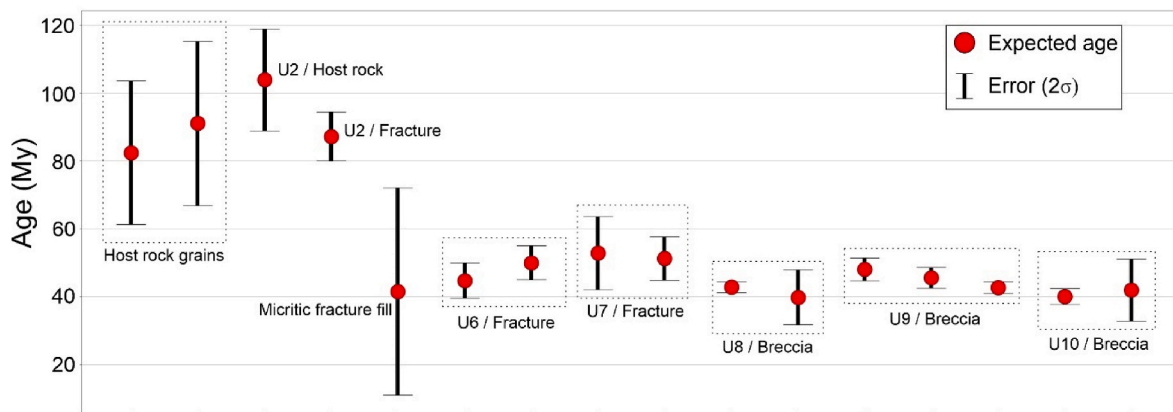


Fig. 12. Distribution of U–Pb ages of calcites in calcite-filled opening-mode fractures, breccias and host rock cements. Two groups of ages can be observed: Older ages (~105–80 Ma) are correlated with the Albo-Cenomanian Durancian uplift; Younger ages (~50–40 Ma) are correlated with the Eocene Pyrenean orogeny. Red circles are the expected age and black bars show the associated absolute error (2σ). (For interpretation of the references to color in this figure legend, the reader is referred to the Web version of this article.)

Table 3

U–Pb ages of analyzed cement phases and host rock.

Sample	Type	Cement phase	Feature	Structure	Age (Ma)	2σ	MSWD	Number of spots
Fc1	Thin section	Host rock	Matrix	Fault core	91.0	24.2	1.1	26
		U2	Fracture (Pre-BR2)		87.2	7.2	4.7	23
		U6	Fracture (Pre-BR2)		44.8	5.1	2.1	28
		U6	Fracture (Pre-BR2)		50.0	5.0	2.0	30
		U8	Breccia pore		42.8	1.6	1.0	24
		U9	Breccia pore		48.1	3.4	1.6	16
Fc2	Thin section	U2	Matrix pore	Fault core	103.8	15.0	2.1	10
Fc3	Billet	U8	Breccia pore	Fault core	39.8	8.1	0.5	23
		U9	Breccia pore		42.7	1.7	1.5	25
		U9	Breccia pore		45.6	3.1	1.5	21
		U10	Fracture (Post-BR2)		41.9	9.2	3.0	21
		U10	Fracture (Post-BR2)		40.0	2.3	1.8	13
Sdz	Billet	U7	Fracture	Damage zone	51.2	6.4	1.3	11
		U7	Fracture		52.8	10.7	1.5	8
		Host rock	Matrix		82.4	21.2	1.6	29
		Micrite	Fracture		41.5	30.5	1.2	42

Ukar and Laubach, 2016; Roberts and Holdsworth, 2022). By contrast, blocky calcite cement is less reliable since deposition of calcite may have occurred late with respect to deformation (post-kinematic). We found syn-kinematic, crack-seal textures in one sample (Fig. 7h). However, cements in most of the studied fractures are blocky. Thus, the U–Pb ages obtained for calcite cements in this study are indicative of the timing when the fractures became occluded by cement rather than the time of deformation. However, the fact that cementation is coincident with the timing of the two main orogenies that affected these rocks strongly suggest that cementation occurred soon after fracturing.

Further valuable thermo-chronometric information about the fault zone history could be acquired using clumped isotope thermometry ($\Delta 47$) linked to U–Pb geochronology data (e.g., Mangenot et al., 2018; MacDonald et al., 2019). Substantial success using this methodology was obtained studying thrust faults in the Pyrenees (e.g. Hoareau et al., 2021; Cruset et al., 2020; Muñoz-López et al., 2022). Another possible study would be to employ Electron Backscattered Diffraction (EBSD) or calcite twin analyses in slickensides to identify major shortening directions associated with fault movement (e.g., Nuriel et al., 2019). This could provide further evidence to correlate local deformation and regional events, or to further separate the cement phases into subgroups. Although these analyses were not included in this study, they are suitable to be applied in this area by future research.

5.2. Cementation and fault permeability

Many authors have used U–Pb calcite geochronology to precisely date the age of brittle deformation (Goodfellow et al., 2017; Nuriel et al., 2019). Another important application of calcite mineralization dating in fractures or fault breccias is to constrain the history of fluid flow in fault zones, since the obliteration of pores and fractures by calcite is linked to the loss of poro-permeability (e.g., Dimmen et al., 2017).

We infer that the Castellás fault had two main phases of brittle deformation that created open fractures before becoming subsequently filled with calcite: one older phase at ca. 90 Ma (e.g. fractures filled with cement U2) that correlates with the Durancian uplift and a younger reactivation phase at ca. 50–40 Ma that correlates with the Pyrenean orogeny (e.g. fractures and breccia filled with U6–U10). Due to the impossibility to date intermediate cement phases (U3, U4 and U5) we lack information about the behavior of the fault zone between these two tectonic episodes.

Further considerations about the fracture network permeability can be drawn based on the presence of micritic sediment deposited within several open Set 2 fractures. The micritic infill (Fig. 7b, f, g, h, Fig. 9a) is intercalated with several Pyrenean cements (U7, U8, U9) and the micritic sediment age indicates a Pyrenean age (Sample Sdz - 41.5 ± 30.5 Ma) (Fig. 11a). The origin of the micrite is most likely allochthonous since there is no micrite in the host rock. This suggests that at some point during the Pyrenean orogeny, the fracture network was permeable

and carrying fluids with suspended sediments, just before further cementation filled all available fracture pore space. The presence of micritic infill in fractures could be associated with precipitation of calcite from overpressurized supersaturated fluids (e.g., Salomon et al., 2021). However, host rock clasts, quartz and asymmetric micritic inclusions in calcite crystals mixed within the micrite (Fig. 7b) suggest that the micritic sediment is allochthonous and infiltrated the fault zone through the fracture network in a shallow burial environment. Petrographical evidence of pendant cement (U8) and sediment infiltration (in U7 and U9) strengthens interpretation of a shallow burial position during Pyrenean reactivation, possibly within the vadose zone. Our isotope dataset does not allow interpretation of fluid origin, but the shift in $\delta^{13}\text{C}$ towards negative values in young cements U9 and U10 (Fig. 10) can be related to interaction with organic matter possibly through the soil (e.g. James and Choquette, 1984), suggesting shallow burial during deposition of these cement phases. Further interpretation about fluid characteristics could be enhanced by calculating fluid isotopic composition, using stable O and C isotopes from calcite cements with estimated fluid temperature from fluid inclusion microthermometry (e.g. Lacroix et al., 2014) or clumped isotope thermometry (e.g. Hoareau et al., 2021; Cruset et al., 2020; Muñoz-López et al., 2022). We did not find suitable fluid inclusions for microthermometry in our samples, but the application of clumped isotope thermometry must be investigated by future research.

Crack-seal textures observed in some of the sediment-filled fractures (Fig. 7h) indicate cementation was synchronous with fracture opening, the Pyrenean U–Pb age in this cases is therefore indicative of the timing of actual deformation. Crack-sealing further suggests that these fractures were prone to reactivation, probably due to their lower mechanical strength (e.g. Clark et al., 1995; Caputo et al., 1998; Hooker et al., 2012; Laubach et al., 2019).

Prior to being filled, open fractures would have acted as conduits but once sealed they would be barriers to fluid flow. Progressive Castellás fault zone evolution created open fractures that most likely enhanced local flow conductivity. By importing material mixed with fluids, enhanced flow may have accelerated cementation within the fault zone (e.g., Dimmen et al., 2017), but repeated cracking created new pathways at each deformational increment. This process explains why the fault zone is intensely cemented today, while the surrounding host rock is porous. We infer the age of U9–U10 cements (c.a. 40 Ma to 48.1 Ma), the youngest dated cement phases, to indicate the time when Pyrenean fractures and fault breccias (BR2) became pervasively cemented (e.g., Fig. 7c and d) turning the fault zone into a permanent barrier for fluid flow.

5.3. Conceptual evolution model

Based on structural, petrographic, isotopic, and geochronological data obtained in this and previous studies (e.g. Matonti et al., 2012; Aubert et al., 2020), we interpret two main stages of deformational-diagenetic development of the Castellás fault zone, which impacted fluid-flow behavior (Fig. 13). Because most of the diagenetic history preserved in these rocks pertains to Set 2 fractures and fault breccias, this discussion focuses on the evolutionary stages after formation of regional, early Set 1 fractures and associated cements.

During the first stage at ~90 Ma the Castellás fault underwent normal slip associated with the Durancian uplift (Fig. 13a). Fault-parallel Set 2 fractures were created in the fault damage zone and BR1 breccias developed in zones of intense deformation within the fault core. Some parts of Set 2 fracture walls follow the outline of host rock grains, suggesting that at least some Set 2 fractures formed when the host rock was under-consolidated. U1–U2 cements filled intergranular pore space in the host rock and porosity in fractures within the damage zone, but affected the host rock outside the fault zone in a mild way. The fine micritic matrix (possibly cataclastic) among clasts in BR1 breccias most likely reduced fault-perpendicular permeability (e.g., Laubach et al., 2014; Haines et al., 2016; Ferraro et al., 2020). However, the sparsity of BR1 breccias in outcrop (Matonti et al., 2012) suggests the fault was segmented at this time (Aubert, 2020), probably allowing fault-perpendicular flow in areas where the low permeability fault core was not present (e.g., Caine et al., 1996).

The second stage at ~50–40 Ma (Fig. 13b) depicts the strike-slip reactivation phase of the Castellás fault during the Pyrenean orogeny. This reactivation led to several phases of calcite-filled opening-mode fractures that enhanced permeability in the damage zone again before becoming filled by younger cements. Continued deformation created a porous mosaic breccia (BR2) consisting of clasts of host rock and BR1. Together the porous breccia BR2 and fractured damage zone could have enhanced fault zone permeability in both fault-perpendicular and fault-parallel directions. Oxides deposited around breccia clasts reported by Aubert et al. (2020) are also suggestive of a permeable fault zone at this time.

During reactivation, fault rocks experienced repeated breakage and cementation, as evidenced by several phases of cross-cutting fractures some of which contain synkinematic cement. At this stage, the fault zone was at a shallow burial position as evidenced by sediment inclusions in U7 and U9, and the pendant shape of U8, with possible vadose influence. Despite widespread cementation, large amounts of sediment infiltration indicate the fault zone was permeable until at least precipitation of U9 cement. Pyrenean cements are absent in the host rock, however,

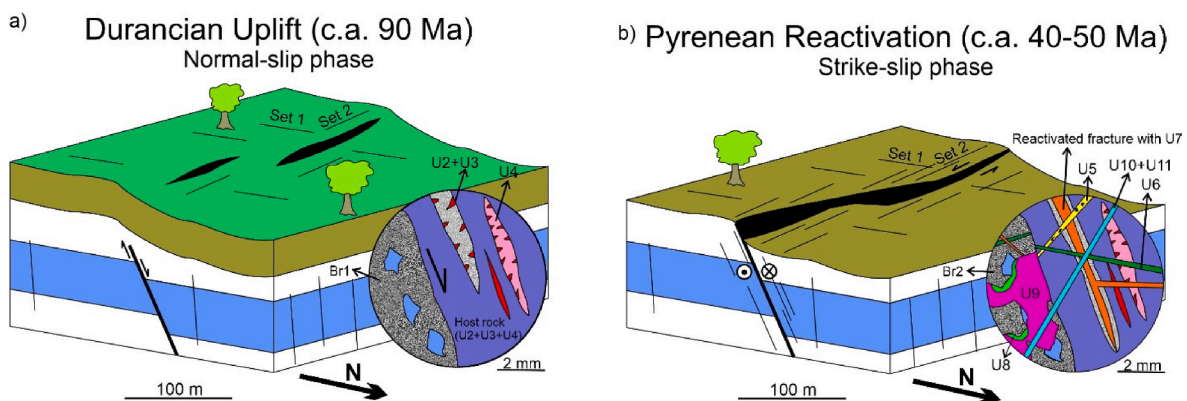


Fig. 13. Two stages of fault zone development anchored in U–Pb ages. Microscale zoom shown inside circle. a) First stage at 90 Ma during the Durancian uplift created a normal fault with permeable fractures and a tight fault core. Fractures likely created a permeable network, but cataclastic fault core may have worked as a baffle for fault-perpendicular flow. Cementation took place shortly after brittle deformation closing fluid pathways with calcite cements. b) Second stage at 40–50 Ma during the Pyrenean orogeny reactivation created a strike-slip fault with permeable fractures and fault core, followed by pervasive cementation in a shallow burial diagenetic environment.

suggesting that the host rock outside of the Castellás fault was most likely impermeable compared to the fault zone. Additional younger deformation occurred subsequently as recorded by narrow calcite-filled opening-mode fractures filled with U10 and U11 cement phases. The lack of young cements in the host rock and BR2 breccia pores indicates they were probably thoroughly cemented by this time.

The Castellás fault zone today is 13.3 m wide in the study area and outcrops as a high ridge, composed of very tight fractured carbonates. The structural-diagenetic evidence preserved in the rocks indicates that little deformation (other than erosion) has occurred in the area since the Pyrenean orogeny.

6. Conclusions

Our study is a rare example that documents evidence for polyphase relative and absolute timing of fracturing, brecciation and subsequent porosity occlusion by cement fills in a fault zone. The evolution of the Castellás fault exemplifies how fault zones in carbonate rocks can change their permeability behavior over time, potentially impacting fluid flow in the subsurface differently by either creating new conduits or by sealing existing fluid pathways due to preferential cementation. Petrographic, isotopic, and U–Pb geochronological data show that the Castellás fault zone underwent two main deformational events during the Durancian uplift (~90 Ma) and Pyrenean orogeny (50–40 Ma). An abundance of fault-parallel, opening-mode fractures created during fault zone reactivation provided pathways for fluid flow during each deformational event. During the Durancian deformational stage, the fault zone had a permeable damage zone and tight, segmented fault core. During the Pyrenean orogeny, both fault core and damage zone were permeable at shallow depths as indicated by sediment inclusions along reactivated fractures due to shallow burial. Fluid flow was permanently prevented due to thorough cementation by ~40 Ma giving place to the mostly impermeable fault rock we see today. Despite representing an important regional deformational event, we found no fracturing that correlates with the Miocene Alpine orogeny, suggesting that most of the Castellás fault zone deformation occurred before then with no recent reactivation.

Local aspects including width of the fault core, degree of cementation, differences in fault throw and facies variation will all influence the localized behavior of the Castellás and similar carbonate fault zones at different points in time. Similar in-depth studies of the structural-diagenetic evolution of fault zones are thus essential to help understand the evolution of permo-porous heterogeneities in fault zones and their sealing/conductive effect on subsurface reservoirs.

Credit author statement

Rodrigo Corrèa: Conceptualization, methodology, software,

Appendix

Here we show additional information about the LA-ICP-MS analysis and U–Pb dating. Table A shows the metadata from the LA-ICP-MS analysis and figures A and figures B show the resulting Tera-Wasserburg diagrams for the U–Pb geochronology using billets and thin sections.

Table A

Metadata for LA-ICP-MS U–Pb geochronology of calcite.

Laboratory name	UTChron Lab, University of Texas at Austin
Sample type/mineral	Calcite
Sample preparation	Polished rock billets/Thin sections
LASER ABLATION SYSTEM	
Make, Model and type	Analyte G2 Excimer Laser Ablation System by Teledyne
Ablation cell	HelEx II 2-vol ablation cell
Laser wavelength (nm)	193 m

validation, formal analysis, investigation, resources, data curation, writing—original draft preparation, writing—review and editing, visualization, project administration. **Estibalitz Ukar:** Conceptualization, methodology, validation, formal analysis, investigation, resources, writing—original draft preparation, writing—review and editing, visualization, supervision. **Stephen Laubach:** Conceptualization, validation, resources, writing—original draft preparation, writing—review and editing, supervision, project administration, funding acquisition. **Irene Aubert:** validation, resources, writing—review and editing. **Juliette Lamarche:** validation, resources, writing—review and editing, project administration. **Qiqi Wang:** validation, writing—original draft preparation, writing—review and editing. **Daniel Stockli:** validation, formal analysis, data curation, writing—review and editing. **Lisa Stockli:** validation, formal analysis, data curation, writing—review and editing. **Toti Larson:** validation, formal analysis, data curation, writing—review and editing.

Funding

This study was funded by Petrobras and by grant DE-FG02-03ER15430 from Chemical Sciences, Geosciences and Biosciences Division, Office of Basic Energy Sciences, Office of Science, U.S. Department of Energy. Our work on fractures is partly supported by the Fracture Research and Application Consortium at The University of Texas at Austin. Field work was facilitated by a research grant to J.E. Olson from the GDL Foundation.

Declaration of competing interest

The authors declare that they have no known competing financial interests or personal relationships that could have appeared to influence the work reported in this paper.

Data availability

Data will be made available on request.

Acknowledgments

We thank Elizabeth Catlos for allowing access to the cold cathodoluminescence device, Charles Kerans for discussions during petrographic analysis, Andras Fall for assistance with sample preparation, and Qilong Fu for allowing access to the microdrill, and Evan Sivil for assistance with O–C isotopic analysis. We want to thank reviewers Andrea Billi, Eric Salomon, and editor Nicolas Beaudoin for providing valuable suggestions. We thank Stephanie Forstner, Mahmood Shakiba, Bethany Rysak and Eric Goldfarb for assistance during field work.

(continued on next page)

Table A (continued)

Pulse width (ns)	5 ns
Fluence (J.cm-2)	4.08 J.cm-2
Repetition rate (Hz)	10 Hz; 6 mJ
Pre-ablation	4 shots before each ablation
Gas blank	27 s
Ablation duration (secs)	30 s
Spot size (mm)	110 µm
Sampling mode/pattern	Static spot ablation
Carrier gas	Helium; 0.65 LPM
ICPMS INSTRUMENT	
Make, Model & type	Thermo Scientific™ Element 2™ High Resolution ICP-MS, single collector magnet sector
Sample introduction	Ablation aerosol
RF power (W)	1250 W
Sample gas flow	0.925 LPM Ar
Detection system	Ion counter
Masses measured	204, 206, 207, 208, 232, 235, 238
Integration time per peak (ms)	2 ms 208,232; 5 ms 202,204,206,238; 8 ms 235; 10 ms 207
Total integration time per reading (secs)	50 ms per pass; 410 runs with 3 passes averaged per run
ICPMS tuning conditions	65 µm line on NIST612: 3.5e6 cps 238U, U/Th = 1.2, UO2/U = 0.09%
DATA PROCESSING	
Sampling strategy	2 standards every 10 unknowns
Calibration strategy	Calcite WC-1 for U–Pb, secondary reference material NIST614; 235U calculated based on 238/235 = 137.88
Reference Material info	WC-1 age: 254.4 ± 6.4 Ma (Roberts et al., 2017)
Data processing package used/Correction for LIEF	Iolite 3.5 with VisualAge_UcomPbine; LIEF correction very small due to 206/238 slope near zero
Common-Pb correction and composition	207 Pbc correction applied to WC-1; 207 Pb/206 Pb = 0.85
Uncertainty level & propagation	Ages in the data table are quoted at 2 sigma (2σ) absolute, calculated from internal reproducibility of reference material

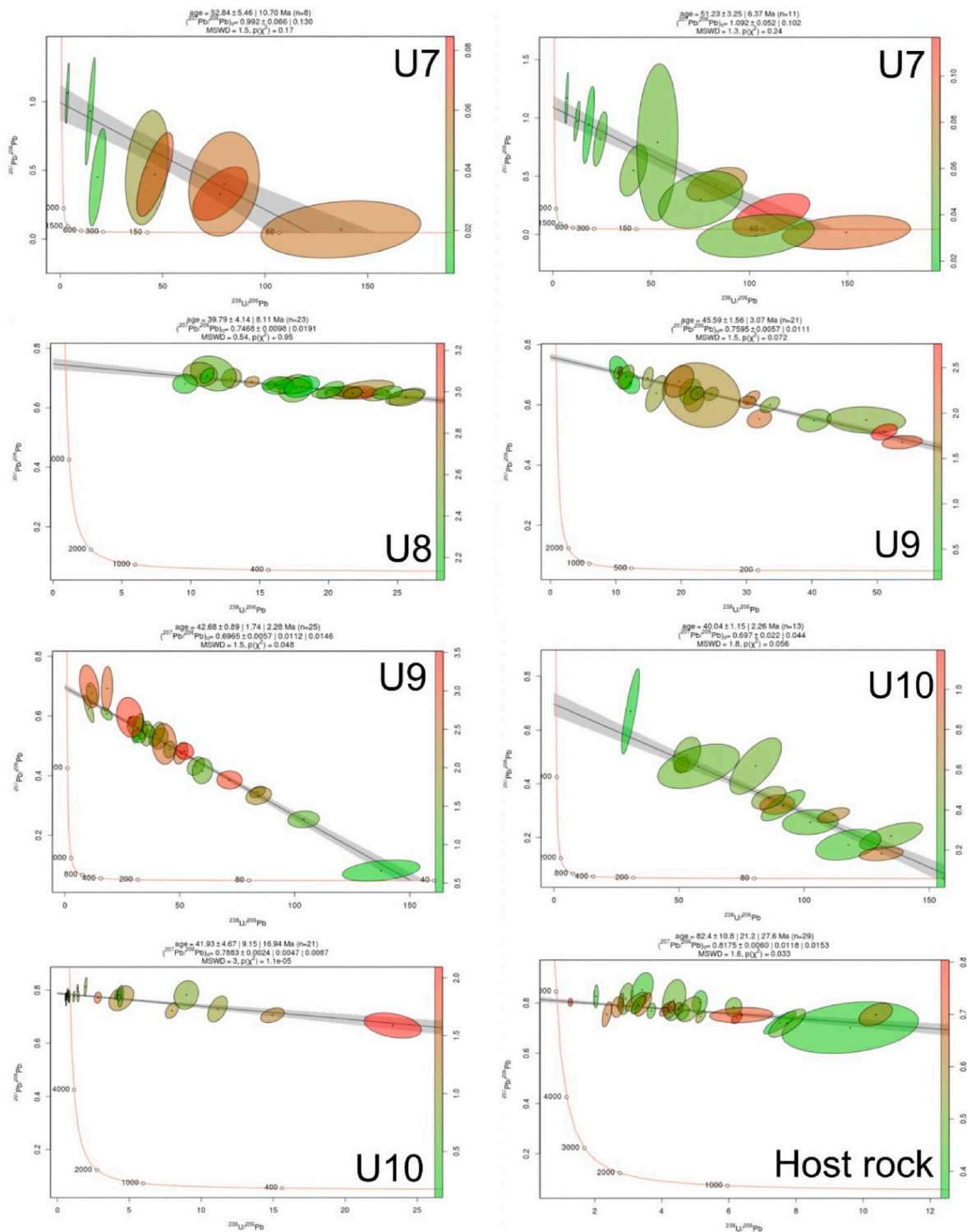


Fig. A. Tera-Wasserburg diagrams for the dated cement phases using billets from samples SDZ and FC3.

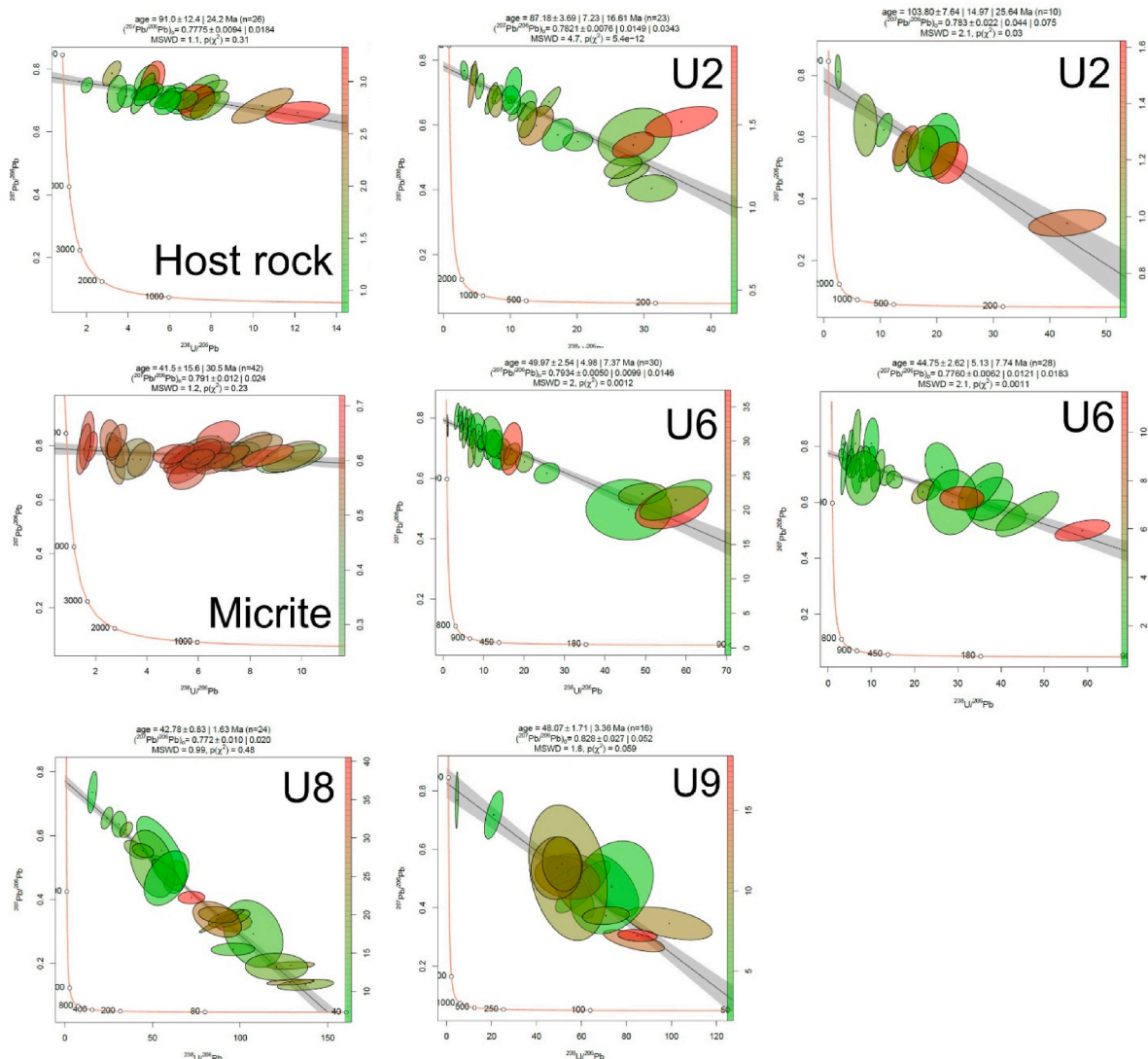


Fig. B. Tera-Wasserburg diagrams for the dated cement phases in thin sections from samples FC1 and FC2.

References

- Aubert, I., Lamarche, J., Léonide, P., 2019. Deciphering background fractures from damage fractures in fault zones and their effect on reservoir properties in microporous carbonates (Urgonian limestones, SE France). *Petrol. Geosci.* 25, 443–453.
- Aubert, I., Léonide, P., Lamarche, J., Salardon, R., 2020. Diagenetic evolution of fault zones in Urgonian microporous carbonates, impact on reservoir properties (Provence-southeast France). *Solid Earth* 11, 1163–1186.
- Aubert, I., 2020. Fault Zone Structural and Diagenetic Evolution in Carbonates - Impact on Reservoir Properties (Urgonian Case Study, SE-France). PhD thesis, Aix Marseille Université.
- Aubert, I., Lamarche, J., Léonide, P., 2021. Ternary fault permeability diagram: an innovative way to estimate fault zones hydraulics. *J. Struct. Geol.* 147, 104349.
- Aydin, A., 2000. Fractures, faults, and hydrocarbon entrapment, migration and flow. *Mar. Petrol. Geol.* 17, 797–814.
- Aydin, A., Eyal, Y., 2002. Anatomy of a normal fault with shale smear: implications for fault seal. *AAPG (Am. Assoc. Pet. Geol.) Bull.* 86, 1367–1381.
- Bagni, F.L., Bezerra, F.H., Balsamo, F., Maia, R.P., Dall'Aglio, M., 2020. Karst dissolution along fracture corridors in an anticline hinge, Jandaíra Formation, Brazil: implications for reservoir quality. *Mar. Petrol. Geol.* 115, 104249.
- Bao, H., Zhai, Y., Lan, H., Zhang, K., Qi, Q., Yan, C., 2019. Distribution characteristics and controlling factors of vertical joint spacing in sand-mud interbedded strata. *J. Struct. Geol.* 128, 103886.
- Bense, V.F., Person, M.A., Chaudhary, K., You, Y., Cremer, N., Simon, S., 2008. Thermal anomalies indicate preferential flow along faults in unconsolidated sedimentary aquifers. *Geophys. Res. Lett.* 35.
- Bestani, L., Espurt, N., Lamarche, J., Floquet, M., Philip, J., Bellier, O., Hollender, F., 2015. Structural style and evolution of the Pyrenean-Provence thrust belt, SE France. *Bull. Soc. Geol. Fr.* 186, 223–241.
- Billi, A., Salvini, F., Storti, F., 2003. The damage zone-fault core transition in carbonate rocks: implications for fault growth, structure and permeability. *J. Struct. Geol.* 25, 1779–1794.
- Billi, A., 2010. Microtectonics of low-P low-T carbonate fault rocks. *J. Struct. Geol.* 32, 1392–1402.
- Bistacchi, A., Mittempergher, S., Martinelli, M., Storti, F., 2020. On a new robust workflow for the statistical and spatial analysis of fracture data collected with scanlines (or the importance of stationarity). *Solid Earth* 11, 2535–2547.
- Bond, C.E., Kremer, Y., Johnson, G., Hicks, N., Lister, R., Jones, D.G., et al., 2017. The physical characteristics of a CO₂ seeping fault: the implications of fracture permeability for carbon capture and storage integrity. *Int. J. Greenh. Gas Control* 61, 49–60.
- Bour, O., Davy, P., Darcel, C., Odling, N., 2002. A statistical scaling model for fracture network geometry, with validation on a multiscale mapping of a joint network (Hornelen Basin, Norway). *J. Geophys. Res.* Solid Earth 107. E7G-4.
- Bussolotto, M., Benedicto, A., Invernizzi, C., Micarelli, L., Plagnes, V., Deiana, G., 2007. Deformation features within an active normal fault zone in carbonate rocks: the Gubbio fault (Central Apennines, Italy). *J. Struct. Geol.* 29 (12), 2017–2037.
- Caine, J.S., Evans, J.P., Forster, C.B., 1996. Fault zone architecture and permeability structure. *Geology* 24, 1025–1028.

- Caputo, R., Hancock, P.L., 1998. Crack-jump mechanism of microvein formation and its implications for stress cyclicity during extension fracturing. *J. Geodyn.* 27, 45–60.
- Chemenda, A.I., Lamarche, J., Matonti, C., Bazalgette, L., Richard, P., 2021. Origin of strong nonlinear dependence of fracture (joint) spacing on bed thickness in layered rocks: mechanical analysis and modeling. *J. Geophys. Res. Solid Earth* 126 (3), e2020JB020656.
- Chew, D.M., Petrus, J.A., Kamber, B.S., 2014. U–Pb LA–ICPMS dating using accessory mineral standards with variable common Pb. *Chem. Geol.* 363, 185–199.
- Choi, J.H., Edwards, P., Ko, K., Kim, Y.S., 2016. Definition and classification of fault damage zones: a review and a new methodological approach. *Earth Sci. Rev.* 152, 70–87.
- Clark, M.B., Brantley, S.L., Fisher, D.M., 1995. Power-law vein-thickness distributions and positive feedback in vein growth. *Geology* 23, 975–978.
- Cochard, J., Léonide, P., Borgomano, J., Guglielmi, Y., Massonnat, G., Rolando, J.P., et al., 2021. Reservoir properties of Barremian–Aptian urgonian limestones, SE France, part 2: influence of diagenesis and fracturing. *J. Petrol. Geol.* 44, 97–114.
- Cruset, D., Cantarero, I., Benedicto, A., John, C.M., Vergès, J., Albert, R., et al., 2020. From hydroplastic to brittle deformation: controls on fluid flow in fold and thrust belts. Insights from the Lower Pedraforca thrust sheet (SE Pyrenees). *Mar. Petrol. Geol.* 120, 104517.
- Dichiarante, A.M., McCaffrey, K.J., Holdsworth, R.E., Bjørnarå, T.I., Dempsey, E.D., 2020. Fracture attribute scaling and connectivity in the Devonian Orcadian Basin with implications for geologically equivalent sub-surface fractured reservoirs. *Solid Earth* 11, 2221–2244.
- Dimmen, V., Rotevatn, A., Peacock, D.C., Nixon, C.W., Nærland, K., 2017. Quantifying structural controls on fluid flow: insights from carbonate-hosted fault damage zones on the Maltese Islands. *J. Struct. Geol.* 101, 43–57.
- Du Bernard, X., Labaume, P., Darcel, C., Davy, P., Bour, O., 2002. Cataclastic slip band distribution in normal fault damage zones, Nubian sandstones, Suez rift. *J. Geophys. Res. Solid Earth* 107. ETG-6.
- Duwiguet, H., Arbaret, L., Guillou-Frottier, L., Heap, M.J., Bellanger, M., 2019. On the geothermal potential of crustal fault zones: a case study from the Pontgibaud area (French Massif Central, France). *Geoth. Energy* 7, 33.
- Evans, J.P., Forster, C.B., Goddard, J.V., 1997. Permeability of fault-related rocks, and implications for hydraulic structure of fault zones. *J. Struct. Geol.* 19, 1393–1404.
- Ferraro, F., Grieco, D.S., Agosta, F., Prosser, G., 2018. Space-time evolution of cataclasis in carbonate fault zones. *J. Struct. Geol.* 110, 45–64.
- Ferraro, F., Agosta, F., Ukar, E., Grieco, D.S., Cavalcante, F., Belviso, C., Prosser, G., 2019. Structural diagenesis of carbonate fault rocks exhumed from shallow crustal depths: an example from the central-southern Apennines, Italy. *J. Struct. Geol.* 122, 58–80.
- Ferraro, F., Agosta, F., Prasad, M., Vinciguerra, S., Violay, M., Giorgioni, M., 2020. Pore space properties in carbonate fault rocks of peninsular Italy. *J. Struct. Geol.* 130, 103913.
- Gattacceca, J., Deino, A., Rizzo, R., Jones, D.S., Henry, B., Beaudoin, B., Vadeboin, F., 2002. Miocene rotation of Sardinia: new paleomagnetic and geochronological constraints and geodynamic implications. *Earth Planet Sci. Lett.* 258 (3–4), 359–377.
- Gillespie, P.A., Howard, C.B., Walsh, J.J., Watterson, J., 1993. Measurement and characterisation of spatial distributions of fractures. *Tectonophysics* 226, 113–141.
- Godeau, N., Deschamps, P., Guihou, A., Leonide, P., Tendil, A., Gerdes, A., Hamelin, B., Girard, J.P., 2018. U–Pb dating of calcite cement and diagenetic history in microporous carbonate reservoirs: case of the Urganian Limestone, France. *Geology* 46 (3), 247–250.
- Goodfellow, B.W., Viola, G., Bingen, B., Nuriel, P., Kylander-Clark, A.R., 2017. Palaeocene faulting in SE Sweden from U–Pb dating of slickenfibres calcite. *Terra Nova* 29 (5), 321–328.
- Guyonnet-Benaize, C., Lamarche, J., Masse, J.P., Villeneuve, M., Viseur, S., 2010. 3D structural modelling of small-deformations in poly-phase faults pattern. Application to the Mid-Cretaceous Durance uplift, Provence (SE France). *J. Geodyn.* 50, 81–93.
- Haines, T.J., Michie, E.A., Neilson, J.E., Healy, D., 2016. Permeability evolution across carbonate hosted normal fault zones. *Mar. Petrol. Geol.* 72, 62–82.
- Hansman, R.J., Albert, R., Gerdes, A., Ring, U., 2018. Absolute ages of multiple generations of brittle structures by U–Pb dating of calcite. *Geology* 46 (3), 207–210.
- Hentschel, H.G.E., Procaccia, I., 1983. The infinite number of generalized dimensions of fractals and strange attractors. *Phys. Nonlinear Phenom.* 8, 435–444.
- Hoareau, G., Crognier, N., Lacroix, B., Aubourg, C., Roberts, N.M., Niemi, N., et al., 2021. Combination of $\Delta 47$ and U–Pb dating in tectonic calcite veins unravel the last pulses related to the Pyrenean Shortening (Spain). *Earth Planet Sci. Lett.* 553, 116636.
- Holdsworth, R.E., McCaffrey, K.J.W., Dempsey, E., Roberts, N.M.W., Hardman, K., Morton, A., et al., 2019. Natural fracture propping and earthquake-induced oil migration in fractured basement reservoirs. *Geology* 47 (8), 700–704.
- Hooker, J.N., Gomez, L.A., Laubach, S.E., Gale, J.F.W., Marrett, R., 2012. Effects of diagenesis (cement precipitation) during fracture opening on fracture aperture-size scaling in carbonate rocks. *Geol. Soc. Lond. Spec. Publ.* 370, 187–206.
- James, N., Choquette, P., 1984. Diagenesis of limestones—the meteoric diagenetic environment. *Geosci. Can.* 11 (4), 161–194.
- Kampman, N., Burnside, N.M., Shipton, Z.K., Chapman, H.J., Nicholl, J.A., Ellam, R.M., Bickle, M.J., 2012. Pulses of carbon dioxide emissions from intracrustal faults following climatic warming. *Nat. Geosci.* 5, 352–358.
- Kim, Y.S., Peacock, D.C., Sanderson, D.J., 2004. Fault damage zones. *J. Struct. Geol.* 26 (3), 503–517.
- Knipe, R.J., Jones, G., Fisher, Q.J., 1998. *Faulting, Fault Sealing and Fluid Flow in Hydrocarbon Reservoirs: an Introduction*, vol. 147. Geological Society, London vols. ii–xxi.
- Lacroix, B., Travé, A., Buatier, M., Labaume, P., Vennemann, T., Dubois, M., 2014. Syntectonic fluid-flow along thrust faults: example of the South-Pyrenean fold-and-thrust belt. *Mar. Petrol. Geol.* 49, 84–98.
- Lamarche, J., Lavenu, A.P., Gauthier, B.D., Guglielmi, Y., Jayet, O., 2012. Relationships between fracture patterns, geodynamics and mechanical stratigraphy in Carbonates (South-East Basin, France). *Tectonophysics* 581, 231–245.
- Laubach, S.E., Eichhubl, P., Hargrove, P., Ellis, M.A., Hooker, J.N., 2014. Fault core and damage zone fracture attributes vary along strike owing to interaction of fracture growth, quartz accumulation, and differing sandstone composition. *J. Struct. Geol.* 68, 207–226.
- Laubach, S.E., Lamarche, J., Gauthier, B.D.M., Dunne, W.M., Sanderson, D.J., 2018. Spatial arrangement of faults and opening-mode fractures. *J. Struct. Geol.* 108, 2–15. <https://doi.org/10.1016/j.jsg.2017.08.008>.
- Laubach, S.E., Lander, R.H., Bonnell, L.M., Olson, J.E., Reed, R.M., 2004. *Opening Histories of Fractures in Sandstone*, vol. 231. Geological Society, London, Special Publications, pp. 1–9.
- Laubach, S.E., Lander, R.H., Criscenti, L.J., Anovitz, L.M., Urai, J.L., Pollyea, R.M., Hooker, J.N., Narr, W., Evans, M.A., Kerisit, S.N., Olson, J.E., 2019. The role of chemistry in fracture pattern development and opportunities to advance interpretations of geological materials. *Rev. Geophys.* 57 (3), 1065–1111.
- Léonide, P., Fournier, F., Reijmer, J.J., Vonhof, H., Borgomano, J., Dijk, J., Rosenthal, M., van Goethem, M., Cochard, J., Meulenaars, K., 2014. Diagenetic patterns and pore space distribution along a platform to outer-shelf transect (Urganian limestone, Barremian–Aptian, SE France). *Sediment. Geol.* 306, 1–23.
- Li, J.Z., Laubach, S.E., Gale, J.F.W., Marrett, R.A., 2018. Quantifying opening-mode fracture spatial organization in horizontal wellbore image logs, core and outcrop: application to Upper Cretaceous Frontier Formation tight gas sandstones, USA. *J. Struct. Geol.* 108, 137–156.
- MacDonald, J.M., Faithfull, J.W., Roberts, N.M.W., Davies, A.J., Holdsworth, C.M., Newton, M., et al., 2019. Clumped-isotope palaeothermometry and LA-ICP-MS U–Pb dating of lava-pile hydrothermal calcite veins. *Contrib. Mineral. Petrol.* 174 (7), 1–15.
- Mangenot, X., Gasparrini, M., Gerdes, A., Bonifacie, M., Rouchon, V., 2018. An emerging thermochronometer for carbonate-bearing rocks: $\Delta 47$ /(U–Pb). *Geology* 46 (12), 1067–1070.
- Marrett, R., Gale, J.F., Gómez, L.A., Laubach, S.E., 2018. Correlation analysis of fracture arrangement in space. *J. Struct. Geol.* 108, 16–33.
- Masse, J.P., 1976. *Les calcaires urgoniens de Provence (Valanginien–Aptien inférieur) - Stratigraphie, paléontologie, les paléoenvironnements et leur évolution*. Aix-Marseille. Marseille, Thèse de la Faculté des Sciences de Luminy (U2), p. 445.
- Matonti, C., Lamarche, J., Guglielmi, Y., Marié, L., 2012. Structural and petrophysical characterization of mixed conduit/seal fault zones in carbonates: example from the Castellans fault (SE France). *J. Struct. Geol.* 39, 103–121.
- Molliex, S., Bellier, O., Terrier, M., Lamarche, J., Martelet, G., Espurt, N., 2011. Tectonic and sedimentary inheritance on the structural framework of Provence (SE France): importance of the Salon-Cavaillon fault. *Tectonophysics* 501, 1–16.
- Moss, S., Tucker, M.E., 1995. Diagenesis of Barremian–Aptian platform carbonates (the Urganian Limestone Formation of SE France): near-surface and shallow-burial diagenesis. *Sedimentology* 42 (6), 853–874.
- Muñoz-López, D., Cruset, D., Cantarero, I., Benedicto, A., John, C.M., Travé, A., 2020. Fluid Dynamics in a Thrust Fault Inferred from Petrology and Geochemistry of Calcite Veins: an Example from the Southern Pyrenees. *Geofluids*.
- Muñoz-López, D., Cruset, D., Vergès, J., Cantarero, I., Benedicto, A., Mangenot, X., et al., 2022. Spatio-temporal variation of fluid flow behavior along a fold: the Bóixols-Sant Corneli anticline (Southern Pyrenees) from U–Pb dating and structural, petrographic and geochemical constraints. *Mar. Petrol. Geol.* 143, 105788.
- Nuriel, P., Craddock, J., Kylander-Clark, A.R., Uysal, I.T., Karabacak, V., Dirik, R.K., et al., 2019. Reactivation history of the North Anatolian fault zone based on calcite age-strain analyses. *Geology* 47 (5), 465–469.
- Ortega, O.J., Marrett, R.A., Laubach, S.E., 2006. A scale-independent approach to fracture intensity and average spacing measurement. *AAPG (Am. Assoc. Pet. Geol.) Bull.* 90, 193–208.
- Ozkaya, S.I., 2018. FRACOR-software toolbox for deterministic mapping of fracture corridors in oil fields on AutoCAD platform. *Comput. Geosci.* 112, 9–22.
- Parizot, O., Misenard, Y., Haurine, F., Blaise, T., Barbarand, J., Benedicto, A., Sarda, P., 2021. When did the Pyrenean shortening end? Insight from U–Pb geochronology of syn-faulting calcite (Corbières area, France). *Terra Nova* 33 (6), 551–559.
- Paton, C., Hellstrom, J., Paul, B., Woodhead, J., Hergt, J., 2011. Iolite: freeware for the visualisation and processing of mass spectrometric data. *J. Anal. At. Spectrom.* 26 (12), 2508–2518.
- Pyrcz, M.J., 2020. *GeostatsPy, Open source Python package for spatial data analytics, Python Package Index*. available at <https://pypi.org/project/geostatspy/>.
- Questiaux, J.M., Couples, G.D., Ruby, N., 2010. Fractured reservoirs with fracture corridors. *Geophys. Prospect.* 58 (2), 279–295.
- Ramsay, J.G., 1980. The crack–seal mechanism of rock deformation. *Nature* 284, 135–139.
- Rasbury, E.T., Cole, J.M., 2009. Directly dating geologic events: U–Pb dating of carbonates. *Rev. Geophys.* 47 (3).
- Révész, K.M., Landwehr, J.M., 2002. $\delta^{13}C$ and $\delta^{18}O$ isotopic composition of $CaCO_3$ measured by continuous flow isotope ratio mass spectrometry: statistical evaluation and verification by application to Devils Hole Core DH-11 calcite. *Rapid Commun. Mass Spectrom.* 16, 2102–2114.
- Rives, T., Razack, M., Petit, J.P., Rawnsley, K.D., 1992. Joint spacing: analogue and numerical simulations. *J. Struct. Geol.* 14, 925–937.
- Roberts, N.M., Drost, K., Horstwood, M.S., Condon, D.J., Chew, D., Drake, H., et al., 2020. Laser ablation inductively coupled plasma mass spectrometry (LA-ICP-MS)

- U–Pb carbonate geochronology: strategies, progress, and limitations. *Geochronology* 2 (1), 33–61.
- Roberts, N.M., Holdsworth, R.E., 2022. Timescales of faulting through calcite geochronology: a review. *J. Struct. Geol.* 104578.
- Roberts, N.M., Rasbury, E.T., Parrish, R.R., Smith, C.J., Horstwood, M.S., Condon, D.J., 2017. A calcite reference material for LA-ICP-MS U–Pb geochronology. *G-cubed* 18 (7), 2807–2814.
- Roberts, N.M., Walker, R.J., 2016. U–Pb geochronology of calcite-mineralized faults: absolute timing of rift-related fault events on the northeast Atlantic margin. *Geology* 44 (7), 531–534.
- Salomon, E., Rotevatn, A., Kristensen, T.B., Grundvåg, S.A., Henstra, G.A., 2021. Microstructure and fluid flow in the vicinity of basin bounding faults in rifts—The Dombjerg Fault, NE Greenland rift system. *J. Struct. Geol.* 153, 104463.
- Sanderson, D.J., Peacock, D.C., 2019. Line sampling of fracture swarms and corridors. *J. Struct. Geol.* 122, 27–37.
- Salvini, F., Billi, A., Wise, D.U., 1999. Strike-slip fault-propagation cleavage in carbonate rocks: the mattinata fault zone, southern apennines, Italy. *J. Struct. Geol.* 21, 1731–1749.
- Smeraglia, L., Giuffrida, A., Grimaldi, S., Pullen, A., La Bruna, V., Billi, A., Agosta, F., 2021. Fault-controlled upwelling of low-T hydrothermal fluids tracked by travertines in a fold-and-thrust belt, Monte Alpi, southern apennines, Italy. *J. Struct. Geol.* 144, 104276.
- Spötl, C., Vennemann, T.W., 2003. Continuous-flow isotope ratio mass spectrometric analysis of carbonate minerals. *Rapid Commun. Mass Spectrom.* 17, 1004–1006.
- Travé, A., Labaume, P., Calvet, F., Soler, A., 1997. Sediment dewatering and pore fluid migration along thrust faults in a foreland basin inferred from isotopic and elemental geochemical analyses (Eocene southern Pyrenees, Spain). *Tectonophysics* 282 (1–4), 375–398.
- Ukar, E., Laubach, S.E., 2016. Syn-and postkinematic cement textures in fractured carbonate rocks: insights from advanced cathodoluminescence imaging. *Tectonophysics* 690, 190–205.
- Ukar, E., Baqués, V., Laubach, S.E., Marrett, R., 2020. The nature and origins of decimeter-scale porosity in Ordovician carbonate rocks, Halahatang oilfield, Tarim Basin, China. *J. Geol. Soc.* 177, 1074–1091. <https://doi.org/10.1144/jgs2019-156>.
- Underschultz, J.R., Otto, C.J., Bartlett, R., 2005. Formation fluids in faulted aquifers: examples from the foothills of western Canada and the north west shelf of Australia. In: Boulton, P., Kaldi, J. (Eds.), *Evaluating Fault and Cap Rock Seals*, vol. 2. AAPG Hedberg Series, pp. 247–260.
- Vermeesch, P., 2018. IsoplotR: a free and open toolbox for geochronology. *Geosci. Front.* 9, 1479–1493.
- Wang, Q., Laubach, S.E., Gale, J.F.W., Ramos, M.J., 2019. Quantified fracture (joint) clustering in Archean basement, Wyoming: application of the normalized correlation count method. *Petrol. Geosci.* 25, 415–428.
- Woodcock, N.H., Mort, K., 2008. Classification of fault breccias and related fault rocks. *Geol. Mag.* 145, 435–440.